

The Extraordinary Maser Flaring Event in the Massive Protostellar System NGC6334I: Multi-epoch milliarcsecond resolution investigation of the 6.7-GHz Methanol Masers

Jayender Kumar,^{1,2*} Simon P. Ellingsen,^{2,3} Gabor Orosz,⁴ Lucas Hyland,² Chris Phillips,¹ Cormac Reynolds,¹ Gordon MacLeod,⁵

¹*CSIRO Space and Astronomy, ATNF Headquarters, 26 Pembroke Rd, Marsfield, NSW 2122, Australia*

²*School of Natural Sciences, University of Tasmania, Private Bag 37, Hobart, Tasmania 7001, Australia*

³*International Centre for Radio Astronomy Research, The University of Western Australia, 35 Stirling Highway, Crawley WA 6009, Australia*

⁴*Joint Institute for VLBI ERIC, Oude Hoogeveensedijk 4, 7991PD Dwingeloo, The Netherlands*

⁵*Hartebeesthoek Radio Astronomy Observatory, P.O. Box 443, Krugersdorp 1741, South Africa*

Accepted XXX. Received YYY; in original form ZZZ

ABSTRACT

We report the first multi-epoch milliarcsecond resolution imaging of the 6.7-GHz class II methanol maser emission associated with the high-mass protocluster system NGC6334I. The observations cover 4 epochs over a 10-year period between March 2010 and March 2020. We confirm the emergence of a number of new regions of 6.7-GHz methanol maser emission in the molecular gas surrounding NGC6334-MM1, which lies north of the previously known class II methanol maser sites which are associated with NGC6334-MM3 and -MM2. The new maser emission is located close to the strongest (sub)millimetre source in the NGC6334I cluster MM1B which experienced a sudden increase in intensity in 2015, produced by an episodic accretion event. We are able to compare the location and intensity of the 6.7-GHz methanol maser emission before, during, and after the flare, providing new insights into the relationship between maser flares and episodic accretion events in high-mass stars.

Key words: masers – stars:formation – ISM: molecules –stars: flare

1 INTRODUCTION

The details of the processes by which the largest stars form is a long-standing problem in astrophysics (e.g. Mac Low & Klessen 2004; Krumholz 2017; Meyer et al. 2017). A range of theories have been proposed, but observational tests of these remain challenging as high-mass stars form in a cluster environment, deeply embedded within cold molecular gas and evolve on relatively short timescales (Krumholz 2017, e.g.). Episodic accretion is well established for young low-mass protostars (Kenyon et al. 1990; Hartmann & Kenyon 1996; Evans et al. 2009; Moscadelli et al. 2017), but it has recently been identified towards a number of high mass star-forming regions and appears to be a common aspect of the formation process (Meyer et al. 2017). Because of the deeply embedded nature of high-mass star formation, one of the biggest challenges in identifying and studying episodic accretion is the timely detection of the onset of such events. Several studies have established an association between the flaring of interstellar masers and the accretion phenomenon (Moscadelli et al. 2017; Burns et al. 2020) and because of this maser monitoring has become a critical tool to investigate and study accretion bursts in star-forming regions (e.g. MacLeod et al. 2018). One such case of maser flaring has been observed in the protostar NGC6334I, which

is situated in the “mini-star burst” region NGC6334 (Willis et al. 2013).

Not long after the discovery of cosmic masers in 1966, 1665-MHz and 1667 MHz OH maser lines were reported in NGC6334 in 1968 (Weaver et al. 1968). In subsequent infrared continuum observations, NGC6334 was identified as one of the most active star-forming regions in the Milky Way (Harvey & Gatley 1983). Subsequent observations with higher angular resolution have shown that this region houses many young, deeply embedded clusters and proto-clusters (Persi & Tapia 2008; Feigelson et al. 2009; Hunter et al. 2006, 2014).

The proto-cluster NGC6334I has a bolometric luminosity of $\sim 1.7 \times 10^4 L_{\odot}$ (Sandell 2000). This region is at a distance of 1.33 ± 0.12 measured from trigonometric parallax (Wu et al. 2014; Chibueze et al. 2014). Submillimetre observations by Hunter et al. (2006) resolved the NGC6334I region into four smaller regions; a previously well-known ultra-compact HII region (UCHII) which they label MM3 (NGC6334F), two line-rich hot cores MM1 and MM2, and a dust core MM4. The line-rich hot-core MM1 is situated at the origin of a high-velocity bipolar molecular outflow (Leurini et al. 2006; Beuther et al. 2008; Qiu et al. 2011). Of these four-millimetre continuum sources, the brightest UCHII region NGC6334F (G351.42+0.64) has been studied in detail (Rodriguez et al. 1982; Gaume & Mutel 1987; Ellingsen et al. 1996b). This region along with the other three regions MM1, MM2, and MM4 as

* E-mail: jayender.kumar@csiro.au

categorized by (Hunter et al. 2006) forms the region NGC6334I. This region is associated with many different maser transitions; from hydroxyl (OH) (Meeks et al. 1969; Moran & Rodriguez 1980), methanol (CH₃OH) both at 6.7 GHz (Menten 1991) and 12 GHz (Batra et al. 1987), water (H₂O) at 22.2 GHz (Meeks et al. 1969) and a variety of other methanol transitions (Haschick & Baan 1989; Haschick et al. 1989, 1990; Menten & Batra 1989; Ellingsen 2002). A recent study by Chibueze et al. (2021) shows the results of a multi-epoch VLBI relative proper motion measurements of the 22-GHz H₂O maser emission using a combination of the VERA and Korean VLBI Network (KVN) to probe the kinematics of the gas surrounding sub-regions MM1 and MM3 during November 2015 to January 2016 period. Their findings show that the H₂O maser proper motions in the MM1 sub-region are mostly driven by the radio jet of sub-region MM1-B and maser proper motions in the UCHII-W1 region inside the MM3 sub-region are largely driven by the expansion of the MM3 sub-region.

The NGC6334I region hosts one of the strongest 6.7-GHz methanol masers sources in the Galaxy. Many of the maser transitions associated with NGC6334I have shown variability in their spectra since the first time they were first observed (MacLeod et al. 2018; Hunter et al. 2017, 2018; Brogan et al. 2016, 2018). The 6.7-GHz methanol masers were first detected in the paper reporting the discovery of this transition (Menten 1991) and have been regularly observed ever since. The Hartebeesthoek radio telescope has been monitoring the 6.7-GHz methanol maser emission from NGC6334I every 10-14 days since February 1999 (MacLeod et al. 2018). In 2015, MacLeod et al. detected a flare in multiple maser species (methanol, OH, and water) associated with NGC6334I. The flare was most pronounced in the 6.7-GHz methanol masers, with some spectral components showing a factor of 20 increase in intensity. The flare commenced in January 2015, peaking 2015 August 15.

The majority of star formation in the local universe takes place in clusters, but the detailed processes involved remain poorly understood because the protocluster environment is both complex, presenting a range of challenges for both observational and theoretical investigations. Variable rates of mass accretion are well known in isolated low-mass star formation (the FU Orionis phenomenon) and Meyer et al. (2017) predicted on the basis of hydrodynamic simulations that they should also be present in primordial and high-mass (cluster) star formation. The relatively small number of high-mass stars in the Milky Way means that episodic accretion events in this regime are more challenging observationally as they will be less common, generally more distant and within a more complex and deeply embedded environment. It is now thought that monitoring of interstellar masers at centimetre wavelengths may provide one of the most rapid and reliable way of identifying an episodic accretion event in high-mass star formation regions. This is primarily based on a close correlation between flares observed in the 6.7-GHz methanol masers and infrared or millimetre continuum emission in two sources - S255 (Caratti o Garatti et al. 2017) and NGC6334I (Hunter et al. 2017)

In this paper, we report milliarcsecond resolution observations of the 6.7-GHz methanol maser emission associated with NGC6334I at four epochs made with the Long Baseline Array (LBA). The data spans a 10 year period with epochs in 2010 and 2011, 2015 and 2020. The four epochs of very long baseline interferometry data, represent the first time we have information before, during and after a major methanol maser flare event at milliarcsecond resolution. These data, combined with the maser monitoring and multi-wavelength published data on NGC6334I provide new information on the relationship between maser flares and episodic accretion events in high-mass star formation regions.

2 OBSERVATIONS AND DATA CALIBRATION

The Long Baseline Array (LBA) is a southern hemisphere VLBI array operated as a National Facility by the CSIRO and the University of Tasmania. There are typically five or six telescopes participating in most array experiments, with the exact number depending upon the source location, frequency of the observations and telescope availability. In this paper, we have included data from four LBA sessions spread over a period of approximately 10 years. A total of eight different antennas participated in one or more of the sessions (Parkes 64m, Mopra 22m, Ceduna 30m, Hobart 26m, Hartebeesthoek 26m, Warkworth 30m, Katherine 12m and The Australian Telescope Compact Array (ATCA)). The ATCA was used in phased array mode in these observations, with the signals from five of the antennas combined prior to recording. Four epochs of observations of the 6.7-GHz methanol maser emission in NGC6334I were made, with the first in March 2010 and the last in March 2020. The observations have experimental codes V255I, J, Z and AI, respectively. The duration of each session was between 8–22 hours. For the V255Z and V255AI epoch, observations of other methanol maser sources were interleaved with those of NGC6334I, but we only report on the latter here.

The DiFX correlator was used to correlate the data (Deller et al. 2011). The data was recorded in dual circular polarization with the $5_1 - 6_0$ A⁺ transition of methanol (rest frequency 6.6685192 GHz) observed in the baseband data of one of the four 16 MHz IFs. A 2 MHz zoom band was correlated to cover the frequency range of the NGC6334I maser emission at each epoch with 2048 spectral channels, providing a spacing of 0.976 kHz (0.044 km s⁻¹). The only exception was for the March 2020 epoch a 4 MHz zoom band with 4096 channels was utilised. The V255 experiments were primarily intended to make trigonometric parallax observations of southern 6.7-GHz methanol maser sources and so were scheduled such that observations of the maser target were interleaved with regular scans on nearby compact extragalactic continuum sources to provide phase referencing. For the NGC6334I, the extragalactic continuum source selected was unsuitable for phase referencing and so we do not have relative astrometry for the masers between the epochs and so we were not able to investigate the proper motion of the masers. Table 1 list the details of the phase-referenced 6.7-GHz methanol maser observations between March 2010 and March 2020 including the start time and the duration of the observations.

The data were calibrated using the Astronomical Image Processing System (AIPS) software. All four epochs have been reduced using the same VLBI data reduction technique. Flag files from each antenna were applied to exclude data for those time ranges when they were not on the source or there were other issues with the data quality noted during the observations. Corrections for ionospheric delays, Earth Orientation Parameters and the changing parallactic angle over the course of the observations were applied by using AIPS VLBAEPCR and CLCOR tasks. The task CVEL was applied to the data to reposition the maser spectrum in the bandpass and to correct for variation in the Doppler shifts due to the Earth's rotation and orbit. We utilised autocorrelation observations of the 6.7-GHz methanol masers made with the Hartebeesthoek radio telescope to calibrate the amplitude for each epoch of the observations (assuming 3830 Jy for the March 2010 and July 2010 epochs, 4375 Jy for the V255Z epoch and 4094 Jy for the V255AI epoch). The tasks ACCOR and CLCOR were used to correct the data amplitude for incorrect sampler statistics and system equivalent flux density (SEFD). The average uncertainties in the flux amplitudes for the four epochs were 0.32, 0.29, 0.56 and 0.38 Jy/beam respectively. The task SPLIT was used to extract a single autocorrelation spectrum scan for one of the ATCA (the most sen-

[htp]

Table 1. Phase-referenced 6.7-GHz methanol maser observations between March 2010 and March 2020 including the start time and the duration of the observations. The participating stations are the Australia Telescope Compact Array (AT), Ceduna (CD), Katherine (KE), Hartebeesthoek (HH), Hobart (HO), Mopra (MP), Parkes (PA) and Warkworth (WA). Columns 1-2 list the year and date of the observation; column 3 lists the day of the year; columns 4-5 list the UT start time and total duration of the observation; column 6 lists the antennas that participated in the particular observation.

Year	Date	D.O.Y	UT Start	Duration (Hours)	Participating stations
2010	09 March	068	14:13	09	AT, CD, HO, HO, PA
2010	22 July	203	08:11	08	AT, CD, HO, MP, PA
2015	01 October	274	22:00	24	AT, CD, HH, HO, MP, WA
2020	19 March	079	05:26	19	AT, CD, KE, MP, PA, WA

sitive telescope in the array) and the task ACFIT was used to scale the spectra of all antennas and for all time ranges relative to this scan. The resultant amplitude correction or gain was then applied to the cross-correlation maser data for each baseline. FRING applied to a strong, compact calibrator source was used to perform manual phase calibration and this solution was also applied to the maser dataset. FRING was then applied to the same maser spot (spectral velocity channel) and this was used to determine the time-dependent rate for all four epochs. The most compact maser emission was then self-calibrated iteratively and the solutions were applied to all maser data. Finally, spectral cubes with stokes I were made with a channel spacing of 0.976 kHz (0.0044 km s^{-1}).

Table 2 lists the details of the observations and other critical information such as project code, total maser emission region, polarization, bandwidth, spectral resolution, and synthesized beam size.

3 RESULTS AND ANALYSIS

This paper presents four epochs of NGC6334I 6.7-GHz methanol maser images at milliarcsecond resolution which span a time range between March 2010 and March 2020. Of these, the third epoch (October 2015) was collected when the NGC6334I region was experiencing a flaring event. Single dish observations of the 6.7-GHz methanol maser emission in the NGC6334I region prior to 2015 showed it covered the velocity range -12 to -6 km s^{-1} , with the strongest emission towards the most negative velocities (see for example Caswell et al. 2010, where NGC6334I corresponds to $351.417+0.645$ and $351.417+0.646$). The 2015 flare in the NGC6334I 6.7-GHz methanol masers was primarily in the emission towards the most positive velocities. The largest changes were at a velocity of approximately -7 km s^{-1} and the positive limit of the observed emission range expanded by to approximately -4.7 km s^{-1} (see figure 1 of MacLeod et al. 2018).

NGC6334I is a cluster star formation region with multiple sites of high-mass star protostellar or young stellar objects (see e.g. Hunter et al. 2006; Brogan et al. 2016). The first interferometric images of the 6.7-GHz methanol maser emission in NGC6334I were made in 1992 by Norris et al. (1993) and show two sites of emission separated by approximately 2 arcseconds. In this paper, we follow the nomenclature of Hunter et al. (2006); Brogan et al. (2016) based on millimetre/submillimetre continuum emission, which identifies three primary sub-regions which they label MM1 to MM3. Brogan et al. (2016); Hunter et al. (2017) identify MM1 as the brightest region in millimetre continuum emission and find it contains multiple dust cores. On this basis they further divided MM1 into 7 sub-regions, from MM1-A to G. They reported that sub-regions MM1-A, MM1-B and MM1-D are the most dominant, with MM1-B being the brightest. Prior to the 2015 flaring event, there are no reported detections of

6.7-GHz methanol masers associated with MM1. The two regions with associated 6.7-GHz methanol masers present before the 2015 flaring event were MM2 and the ultra-compact HII region MM3 which is also known as NGC6334F. Trigonometric Maser parallax observations of the adjacent core NGC6334I(N) measure a distance of 1.3 kpc and we assume that to also be the distance to NGC6334I (Reid et al. 2014; Chibueze et al. 2014) which implies an angular offset of 1 arcsecond in NGC6334I corresponds to a linear separation of 1300 astronomical units (light-travel time ~ 7.5 days)

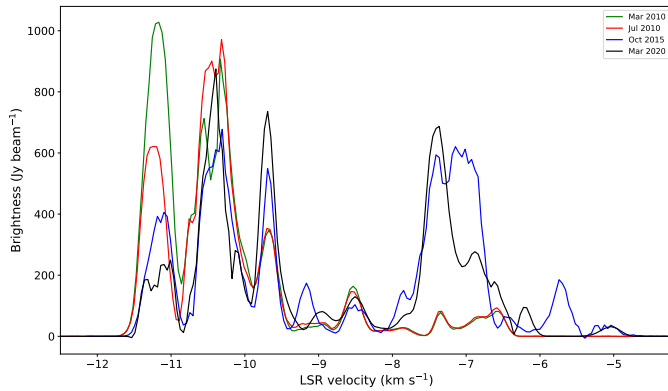
Figure 1 shows a comparison of the 6.7-GHz methanol maser emission spectra for the whole NGC6334I region extracted from the image cubes for all four epochs. It shows that for the 2010 epochs, the strongest emission was in the velocity range -10 to -11.5 km s^{-1} and is around an order of magnitude stronger than that observed in the velocity range -8.0 to -6.5 km s^{-1} . The image-cube spectra for the 2015 and 2020 epochs show significant differences with the emission at the most negative velocities having declined and that at velocities in the -8.0 to -6.5 km s^{-1} range the emission is comparable in intensity to that in the -10 to -11.5 km s^{-1} velocity range. This is consistent with the single dish monitoring results of MacLeod et al. (2018) which show persistent changes in the 6.7-GHz methanol maser spectrum following the approximately year-long flare event.

We have imaged a region of NGC6334I covering 16×16 arcsecond, from a Right Ascension (J2000) of $17:20:53.7$ to $17:20:53$ and a Declination $-35:46:54.0$ to $-35:47:04.0$. Figures 5–8 show the VLBI interferometric spot maps of the 6.7-GHz methanol masers for each of the four epochs, from March 2010 to March 2020. The large angular extent of the 6.7-GHz methanol masers in NGC6334I presents some challenges for imaging at milliarcsecond resolutions. Initial images with a large cell-size were created to identify the total extent and location of the maser emission clusters and this was followed by simultaneous imaging and cleaning with an optimal cell-size of up to 3 fields which covered all the emission apparent in the initial images. This approach is critical to accurately image masers for sources where there is strong emission from different regions which overlaps in velocity. In some cases, the multi-field higher resolution images revealed weaker maser emission towards the edge of a field. When this occurred the field centre or extent was modified in an iterative manner until we were confident that all the maser emission was captured. The three main NGC6334I regions; MM1, MM2 and MM3 are labelled in each of the spot maps. The spot maps were created by fitting 2D Gaussian to all components in each channel of the image cubes $> 8\sigma$. Each circle in the spot map represents a maser feature and is centred at the weighted average of emission where the peak of the 2D Gaussian has a spatial separation than 0.2 mas distance and is within a 0.5 km s^{-1} velocity range. The diameter of the circle is proportional to the integrated flux density. The colour of the circles depends upon the velocity of the maser feature.

The combined affect of different antennas in the array, time on

Table 2. Details of the observations and other information of the observed data of maser region NGC6334I with the LBA array. Column 1 lists the different parameters of the analysed image data cube; columns 2-5 list the corresponding values of those parameters for epochs 1-4

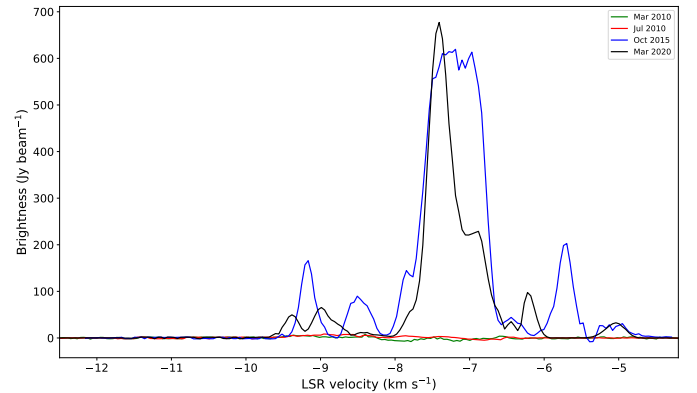
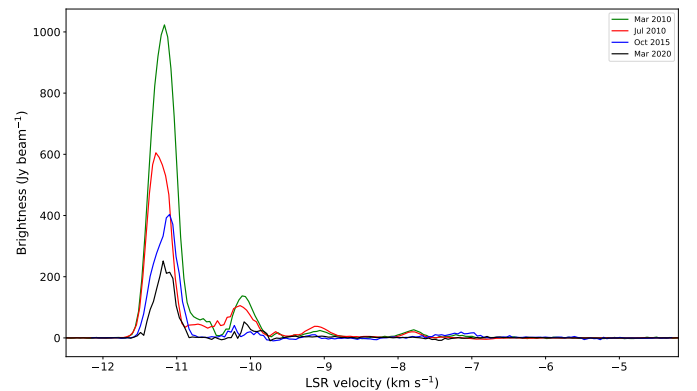
Parameters	Epoch 1	Epoch 2	Epoch 3	Epoch 4
Project Code	V255I	V255J	V255Z	V255AI
Observing Date	09 March 2010	22 July 2010	01 October 2015	19 March 2020
Modified Julian Date	55264	55399	57296	58927
Maser Emission Regions	MM2, MM3	MM2, MM3	MM1(I,II,III), MM2, MM3	MM1(I,II), MM2, MM3
Polarization products	dual circular	dual circular	dual circular	dual circular
Bandwidth	2 GHz	2 GHz	2 GHz	4 GHz
Imaged Field Width (arc sec)	4.096 x 4.096	4.096 x 4.096	4.096 x 4.096	4.096 x 4.096
Cube Spectral Resolution (km s^{-1})	0.44 km s^{-1}	0.44 km s^{-1}	0.44 km s^{-1}	0.44 km s^{-1}
Synthesized Beam (" mas \times mas " (P.A. $^\circ$))	5.43 x 4.45 (68.50 $^\circ$)	4.99 x 4.76 (44.32 $^\circ$)	3.82 x 3.05 (-63.18 $^\circ$)	5.00 x 3.54 (19.44 $^\circ$)
Number of channels in spectral data	2048	2048	2048	4096
RMS noise per channel (Jy beam^{-1}) (median, max, min)	0.357, 1.83, 0.043	0.322, 1.38, 0.043	0.566, 2.9, 0.118	0.308, 1.14, 0.102

**Figure 1.** The interferometric total-power (Stokes-I) spectra of the maser emission extracted from the image cubes for all four epochs. Each epoch's emission spectrum is colour-coded and labelled in the figure.

source and maser intensity means that the noise in the image cubes changes with epoch and velocity. We are interested in the changes in the location and intensity of the maser emission during and after the flare compared to prior to the flare. To facilitate that comparison we have used the same objective criteria to create the spot maps for each epoch. The criteria are that the emission has a signal-to-noise (SNR) ratio greater than 8; an intensity greater than 1 Jy/beam and be present in 3 consecutive velocity channels. Tables A1–A4 in Appendix A lists all the identified maser features for the whole NGC6334I region (MM1, MM2, MM3 regions) for each epoch. For each maser feature the right ascension and declination offsets from the centre position (R.A. = 17:20:53.454, DEC. = -35:47:00.520 [J2000]), velocity, integrated flux density and the region (MM1, MM2 or MM3) it is associated with is specified in the table.

Figures 2-4 show a comparison of the interferometric maser brightness spectra for all three NGC6334I sub-regions: MM1, MM2 and MM3 for all four epochs.

The maser spot maps for the four epochs (Figures 5–8) show 6.7-GHz methanol maser emission associated with each of the three-millimetre continuum sources in the NGC6334I region MM1, MM2 and MM3. There is emission associated with MM2 and MM3 across all four epochs, whereas MM1 only shows emission for the two epochs taken after the commencement of the 2015 flare. In the following sections, we discuss the emission associated with each of the three main sub-regions.

**Figure 2.** The interferometric brightness spectrum of the maser emission from sub-region MM1, extracted from the image cubes for all four epochs. Each epoch's emission spectrum is colour-coded and labelled in the figure.**Figure 3.** The interferometric brightness spectrum of the maser emission from sub-region MM2, extracted from the image cubes for all four epochs. Each epoch's emission spectrum is colour-coded and labelled in the figure.

3.1 Sub-Region MM3

The MM3 region is associated with the well-studied ultra-compact HII region NGC6334F (Rodríguez et al. 1982; Ellingsen et al. 1996a; Hunter et al. 2006; Brogan et al. 2016). Both OH and water maser emission have been detected towards MM3 (Forster & Caswell 1989;

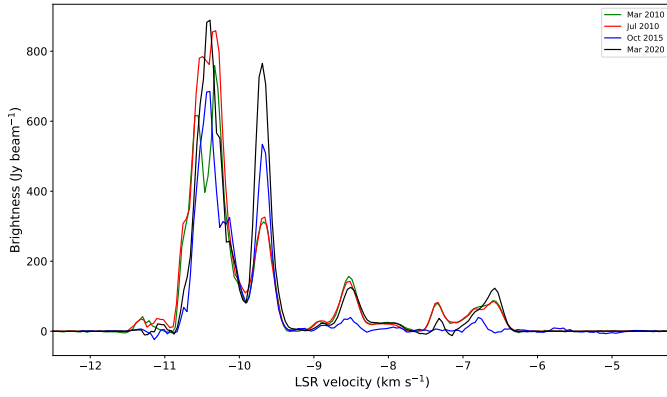


Figure 4. The interferometric brightness spectrum of the maser emission from sub-region MM3, extracted from the image cubes for all four epochs. Each epoch’s emission spectrum is colour-coded and labelled in the figure.

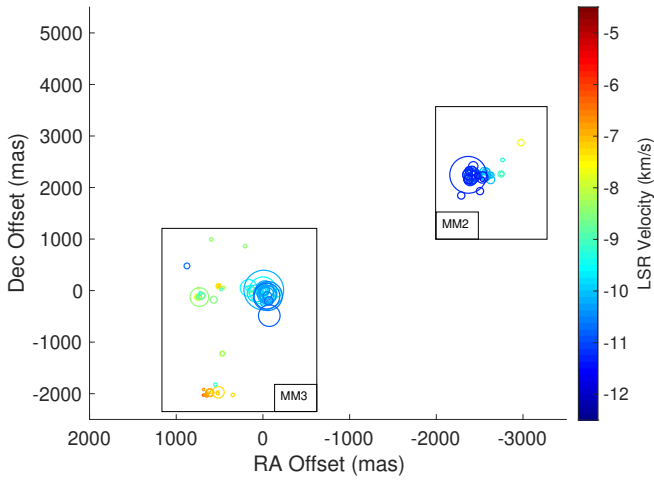


Figure 5. Interferometric spot maps of 6.7-GHz methanol maser features in R. A., DEC. plot for the total maser emission of NGC6334I star-forming region for the March 2010 epoch. All maser features are plotted on the Right Ascension (R.A.) and Declination (DEC.) map with their velocity information. The whole region is further divided into multiple sub-regions based on the nomenclature of (Brogan et al. 2016; Hunter et al. 2017, 2018). Note that there was no emission detected from the MM1 sub-region during this epoch which can also be seen from the lack of any spectral components in Figure 2.

Hunter et al. 2018; Chibueze et al. 2021), in addition to numerous class II methanol maser transitions (Cragg et al. 2001). The MM3 region has generally shown the strongest 6.7 class II methanol maser activity in all previous studies (Menten 1991; Ellingsen et al. 1996b; Walsh et al. 1998; Goedhart et al. 2004; Hunter et al. 2018) and is one of the brightest 6.7-GHz methanol masers in the Milky Way. The strongest class II methanol maser emission from the MM3 region is observed over the velocity range $-11.5 - -9.5 \text{ km s}^{-1}$ and has been confirmed through interferometric imaging for the 6.7, 12.2, 19.9, 23.1, 37.7, 38.3 and 38.5-GHz transitions (Norris et al. 1993; Krishnan et al. 2013; Ellingsen et al. 2018). Figure 4 shows that for all four epochs, there is strong 6.7-GHz methanol maser emission from MM3 in the velocity range from -11 km s^{-1} to -9.3 km s^{-1} . The two

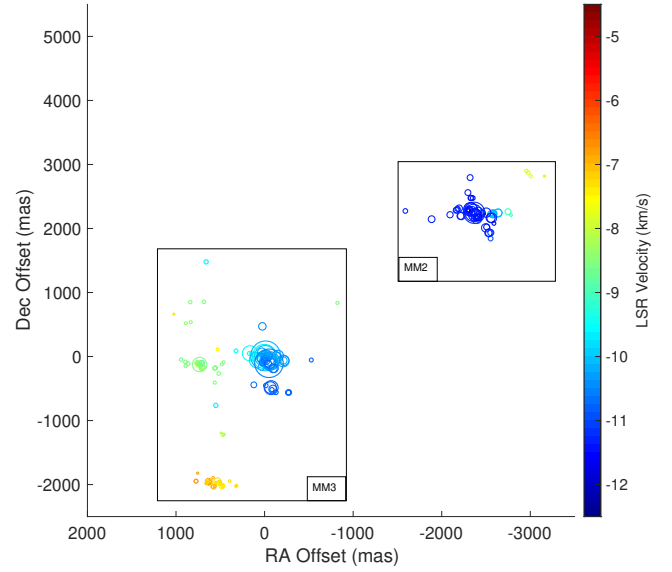


Figure 6. Interferometric spot maps of 6.7-GHz methanol maser features in R. A., DEC. plot for the total maser emission of NGC6334I star-forming region for the July 2010 epoch. All maser features are plotted on the R.A., DEC. map with their velocity information. Similar to the March 2010 epoch, there was no emission detected from the MM1 sub-region during this epoch as well which can also be seen from the lack of any spectral components in Figure 2.

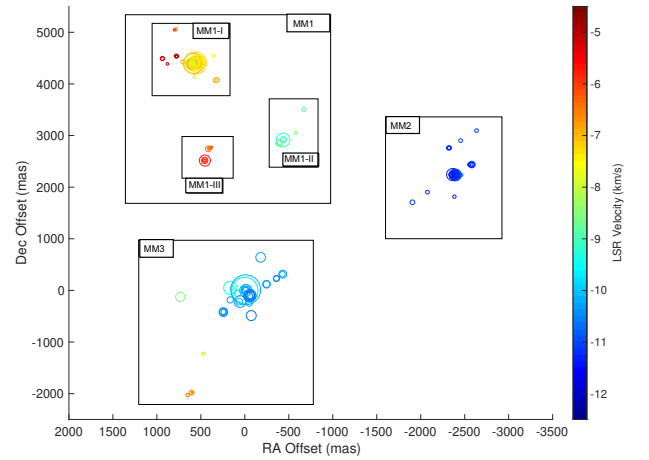


Figure 7. Interferometric spot maps of 6.7-GHz methanol maser features in R. A., DEC. plot for the total maser emission of NGC6334I star-forming region for the October 2015 epoch. All maser features are plotted on the R.A. and DEC. map with their velocity information.

epochs after the commencement of the flare (Oct 2015 and March 2020) do not show the emergence of any new spectral components from the MM3 region, although the relative intensity of the emission has changed significantly over the 10-year duration of these observations. The emission at the most negative velocities shows a significant decrease in intensity following the onset of the flare, while the maser

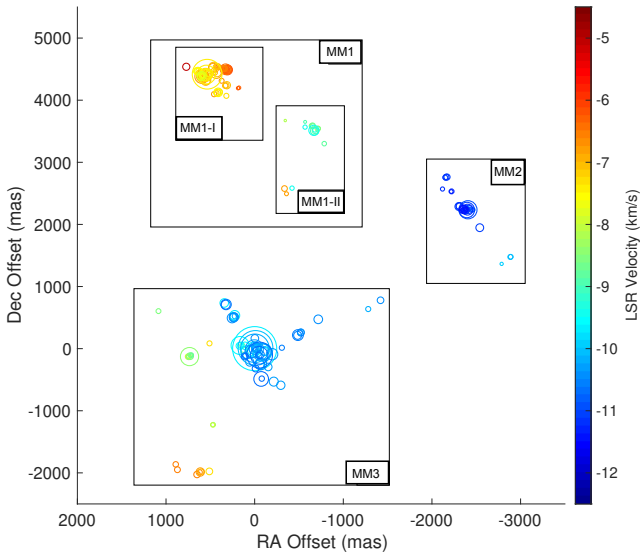


Figure 8. Interferometric spot maps of 6.7-GHz methanol maser features in R. A., DEC. plot for the total maser emission of NGC6334I star-forming region for the March 2020 epoch. All maser features are plotted on the R.A. and DEC. map with their velocity information.

components with peak velocities of approximately -10.4 and -9.7 km s^{-1} increase in intensity. The latter of these is now the brightest milliarcsecond-scale emission in the 6.7-GHz transition associated with NGC6334I and in October 2020 had an intensity approximately a factor of four stronger than a decade earlier. The emission at around -8.6 km s^{-1} shows relatively little variation in intensity over the four epochs and because of that was used to provide the self-calibration at each epoch.

In the interferometric maser spot maps shown in Figures 5–8, the MM3 region shows the 6.7-GHz class II methanol emission covering an area on the sky of approximately 2.3×2.3 arcseconds. The strongest emission in the velocity range from -11 km s^{-1} to -9.3 km s^{-1} is located towards the western edge of the cometary ultra-compact HII region. Emission at velocities around -8 km s^{-1} is located approximately 0.75 arcseconds (1000 au) eastwards and the most positive velocity emission pre-flare (-7.5 km s^{-1} to -6.5 km s^{-1}) located 2 arcseconds (2600 au) south. A comparison of the 6.7-GHz methanol maser associated with the MM3 region over the four epochs of observation shows that the number of components and their angular spread was at its lowest in the October 2015 epoch, at the height of the flare. This may be partly due to the noise level for those data being nearly a factor of two higher than for the other three epochs (and hence it is more likely that weaker maser emission is missed). However, the data are consistent with the maser emission in the MM3 region being partly suppressed or reduced at the same time that it peaked in MM1. The strongest 6.7-GHz methanol maser emission in the MM3 region is separated from the peak of the MM1 continuum emission by approximately 3 arcseconds, corresponding to a light-travel time of around 20 days at the assumed distance of 1.3 kpc. This means that it is plausible that changes in the radiation field of MM1 due to the 2015 flare could be impacting the masers in the MM3 region during the October 2015 epoch. The single dish monitoring data (see figure 1 of MacLeod et al. 2018) does not show evidence of significant time delays across the spectrum, which

suggests that any changes which impact the three 6.7-GHz methanol maser emission regions in NGC6334I are either near-simultaneous compared to the approximately fortnightly observation cadence of MacLeod et al., or are independent.

3.2 Sub-Region MM2

The MM2 region was first identified as a distinct site of maser emission with the detection of 12.2-GHz methanol masers at this location by Norris et al. (1988). The first interferometric observations of 6.7 class II methanol masers in NGC6334I were made in 1992, soon after the discovery of the transition and all subsequent observations have detected strong emission associated with MM2, (Norris et al. 1993; Ellingsen et al. 1996b; Walsh et al. 1998; Hunter et al. 2018). Figure 3 shows that for all four epochs, there is strong emission in the velocity range from -11.6 km s^{-1} to -10.8 km s^{-1} . This emission was strongest in the March 2010 epoch and has shown a consistent decline in intensity in subsequent epochs, although the largest decline occurred well prior to the 2015 flare event. Along with the strong emission, there is weaker emission present in the velocity ranges from -10.4 km s^{-1} to -9.7 km s^{-1} , most of which has significantly declined in the October 2015 epoch but appears to have slightly strengthened in March 2020 epoch. There is also very weak emission in velocity ranges from -9.3 km s^{-1} – -8.8 km s^{-1} and from -8.0 km s^{-1} – -7.6 km s^{-1} in both 2010 epochs, which has disappeared in October 2015 and March 2020 epoch.

In the interferometric maser spot maps shown in Figures 5–8, the MM2 region exhibits 6.7-GHz class II methanol emission over a 1.5×2.5 arcsecond region, which is located approximately 3.25 arcseconds (4200 au) north-west of the strongest methanol maser emission in MM3. Figures 5–8 show significant differences in the distribution of the weaker maser emission in the MM2 region from epoch to epoch. The strongest 6.7-GHz methanol maser emission in the MM3 and MM2 regions overlaps in velocity and some of the changes in maser distribution are likely related to this (even though the interferometric resolution of our observations is several orders of magnitude higher than the separation between the two regions). This is particularly evident during the 2015 outburst event. The March 2020 maser distribution for MM2 also shows significant difference from that seen in pre-flare epochs, however, we cannot determine from our data the degree to which the changes in MM2 are related to external influences (i.e. MM1) or changes in MM2 itself.

3.3 Sub-Region MM1

Prior to the 2015 flaring event there had been no 6.7-GHz class II methanol maser emission detected toward the MM1 region. We have imaged the MM1 region for all four epochs and Figure 2 confirms that in 2010 there was no associated 6.7-GHz methanol maser emission on milliarcsecond scales with an intensity greater than 1 Jy beam^{-1} in the LSR velocity range from -12.0 km s^{-1} to -4.5 km s^{-1} . In contrast, for the October 2015 epoch 6.7-GHz methanol maser emission associated with MM1 is observed over a wide velocity range. The emission is strongest in the velocity ranges -8 km s^{-1} to -6.5 km s^{-1} , with the highest intensity emission peaking at a velocity of around -7.5 km s^{-1} . There are five spectral components in the velocity range -9.5 km s^{-1} to -8.9 km s^{-1} , -8.8 km s^{-1} to -8.1 km s^{-1} , -8.0 km s^{-1} to -6.5 km s^{-1} , -6 km s^{-1} to -5.5 km s^{-1} and -5.4 km s^{-1} to -4.8 km s^{-1} . The single dish monitoring observations of MacLeod et al. (2018) found that commencing in January 2015, methanol emission in this velocity range in the NGC6334I region

started flaring. Our October 2015 epoch was observed at approximately the time the 6.7-GHz methanol maser flare was at its peak intensity.

In the interferometric maser spot maps shown in Figures 5–8, the MM1 region shows 6.7-GHz methanol emission covering a 3×3 -arcsecond region, north of MM3 region. Brogan et al. (2016) reported that this region houses the brightest millimetre continuum emission in the protostellar cluster. With the resolution and sensitivity of ALMA observations, Brogan et al. (2016) identified 7 sub-regions, labelled MM1-A to G, based on the 1.3 mm dust continuum emission. They found that sub-regions MM1-A, MM1-B and MM1-D are the brightest regions in MM1 with MM1-B being the bright and most dominant, but with each a strong candidate to be hosting its own star. Hunter et al. (2018) made VLA A-array observations of the 6.7-GHz methanol masers in NGC6334I in October and November 2016 (approximately a year following the October 2015 LBA observations reported here). Their observations show the strongest 6.7-GHz methanol maser emission associated with the MM1 region is located to the northern edge of the millimetre continuum emission, with the other main clusters to the west in the general direction of the MM2 region.

We found three main regions of 6.7-GHz methanol masers in our October 2015 observations of MM1 and have labelled these MM1-I to MM1-III. Figures 5–8 show the MM1 sub-regions in rectangular boxes for the two later epochs (October 2015 and March 2020 epochs). The centre of the MM1-I region shows the strongest emission from this region. It is offset of ~ 580 mas and 4400 mas in right ascension and declination, respectively, from the centre of the MM3 region.

While the flare in the 6.7-GHz methanol masers associated with MM1 had its peak intensity around August 2015 and the intensity of emission for part of its velocity emission range has subsequently declined, figure 1 of MacLeod et al. (2018) shows post-flare emission in the $-7.5 - -6.5$ km s $^{-1}$ remained substantially stronger than pre-flare levels through to late 2017 (the end of the observations reported in that paper). Figure 8 shows that much of the 6.7-GHz methanol maser emission detected near the peak of the flare in 2015 is still detected five years later in March 2020. In the March 2020 epoch, while the emission range of the main feature has slightly become stronger, the emission in between -9.5 km s $^{-1} - -8.8$ km s $^{-1}$ has significantly reduced and emission in the velocity range -8.8 km s $^{-1} - -8.1$ km s $^{-1}$ and -6.0 km s $^{-1} - -5.5$ km s $^{-1}$ has died down. Interestingly, March 2020 observations show some new emission at around -6.2 km s $^{-1}$. The main differences are in the intensity and location of the components south and west of the main MM1 emission region. The MM1-I cluster shows maser emission over the velocity range -7.5 km s $^{-1}$ to -5.5 km s $^{-1}$. Most of the maser emission in the MM1-I region persisted in the March 2020 observations (Figure 8). The MM1-II region has 6.7-GHz methanol maser emission over the velocity range -9.5 km s $^{-1} - -9$ km s $^{-1}$ and is situated southwest of MM1-I. The maser emission associated with the MM1-II region in our final (March 2020) epoch shows significant evolution from that observed in October 2015. In March 2020 there is significant maser activity in MM1-II over an extended range of velocity, north of that seen in 2015. The 2015 observations show regions of emission to the south of between MM1 in the general direction of MM3 at velocities around -6 km s $^{-1}$, which was not detected in March 2020 and the emission south-west of the MM1 in the general direction of MM2 at velocities of around -9 km s $^{-1}$ also changes between the two epochs to a much greater degree than for most of the other regions. The spectral channels in the velocity range -11.5 km s $^{-1}$ to -10.0 km s $^{-1}$ are affected by sidelobes arising from strong emission

in the neighbouring MM2 and MM3 sub-regions. Due to the large field size and the complexity of the emission structure, the CLEAN process had inherent limitations and was unable to fully mitigate sidelobe contamination at these velocities in MM1. However, this contamination has been accounted for in the analysis and we find no evidence of 6.7 GHz methanol maser emission in MM1 in this velocity range prior to 2015.

3.4 Comparison with Earlier Studies

Figure 9 shows the 6.7-GHz methanol maser distribution in NGC6334I across all four epochs and shows how it has changed. In particular, it highlights the significant changes in the maser clusters to the south and south-west of MM1 between 2015 and 2020 and the change in the extent of the MM2 and MM3 emissions over the 10-year period. Figure 10 compares 6.7-GHz methanol maser emission from the LBA October 2015 epoch with the Hunter et al. (2018) results from VLA observations. Hunter et al. (2018) used the VLA in "A" configuration with data collected over two sessions on October 29, 2016 and November 19, 2016. They recorded the data in dual polarization with a channel spacing of 1.953 kHz (0.0878 km s $^{-1}$) over a span of 90 km s $^{-1}$ centred on an LSR velocity of -7 km s $^{-1}$. The 6.7 GHz VLA data have an angular resolution approximately a factor of 100 lower than the LBA data, but significantly greater sensitivity. Considering the combined effect of different sensitivity, angular resolution and source evolution Figure 10 shows a close agreement between the LBA and VLA distributions. Hunter et al. detected many weak maser components (intensities between 0.01 and 0.05 Jy) in the MM1 region at velocities more positive than -4.2 km s $^{-1}$. We detected some weak emission in this velocity range in the single antenna (autocorrelation) spectra in the October 2015 observations, but this emission was not detected in our VLBI images, showing that as for most 6.7 GHz methanol maser emission a significant fraction is resolved, indicating that these weak features are not unusually compact. In Figure 10, there is a small offset in right ascension between the LBA and VLA distributions. The VLA observations have accurate absolute astrometry, whereas the LBA observations do not due to the selection of a poor phase reference source. The alignment between the two datasets is hence subjective and as they have been reduced and imaged using different data reduction packages (AIPS and CASA), projection effects will also impact relative right ascension separation of components at different velocities.

4 DISCUSSION

NGC6334I is one of the best-studied star formation regions in relation to its maser activity of different species (Weaver et al. 1968). It hosts multiple maser species in the ground state as well as in the excited state. While the first interstellar methanol maser transitions were detected in the early 1970s the field didn't really gain momentum until the mid-1980s with a concerted observational campaign originated by Wilson and Menten at the Max Planck Institut für Radioastronomie which detected many new maser transitions and sources. The most influential of the newly discovered transitions was the 6.7 GHz (Menten 1991), which is the second most common and second strongest interstellar maser transition towards Galactic high-mass star formation regions. NGC6334F was identified as a proto-typical class II methanol maser source in these pioneering observations and the first observation of the 6.7-GHz emission

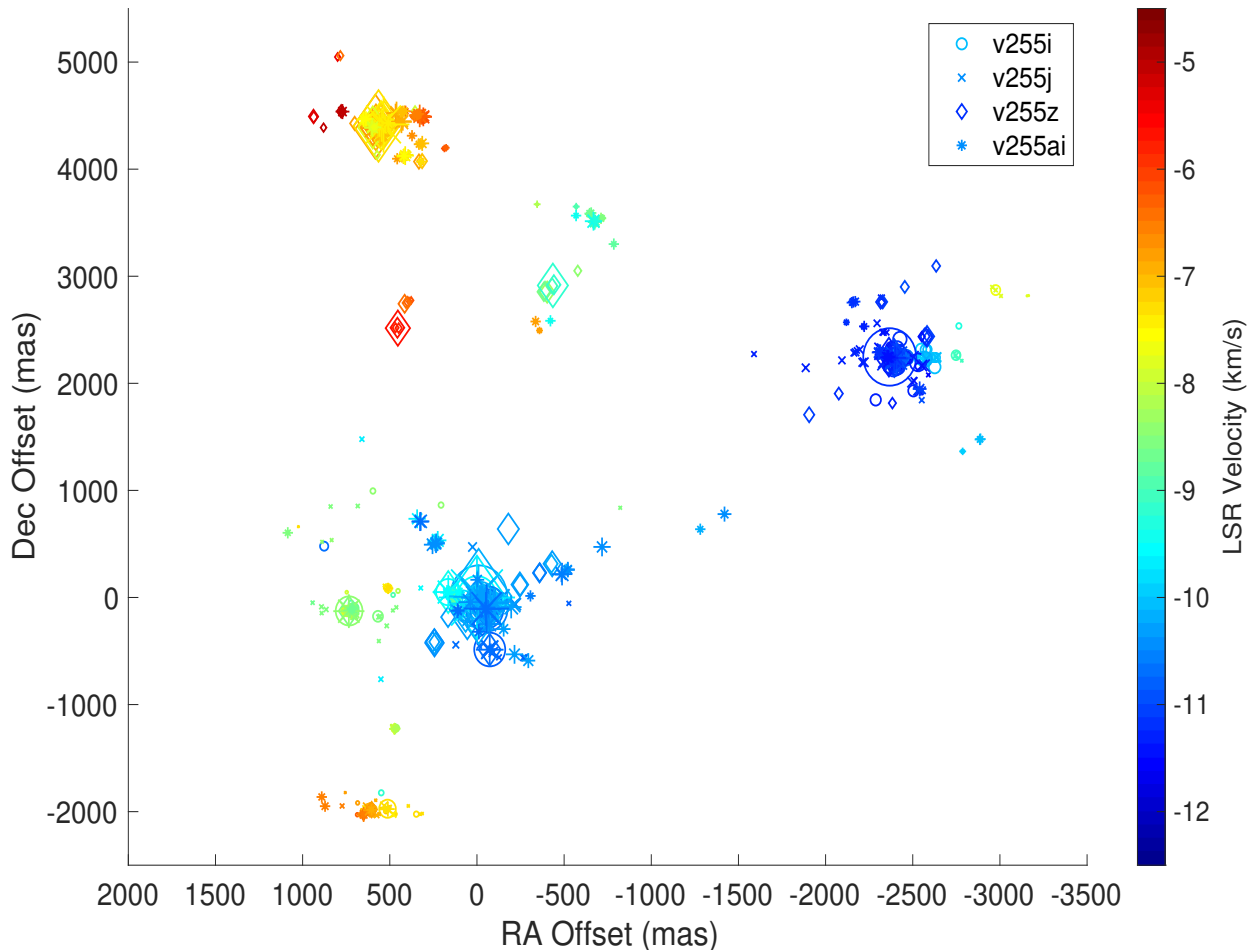


Figure 9. Interferometric map of the total maser emission in NGC6334I star-forming region for all four, March 2010, July 2010, October 2015, March 2020 epochs. All maser features are plotted on the R.A. and DEC. map with their velocity information. Data for each epoch is plotted with a different marker, which is shown on the top left corner of the map.

was undertaken in May/June 1991 and is reported in the discovery paper for this transition (Menten 1991). Observations in 1992 and 1993 reported slight variability in the 6.7-GHz methanol masers in NGC6334F (Caswell et al. 1995b), but it was sufficiently unremarkable that it was not included in the first paper investigating the variability of the 6.7 GHz-transition (Caswell et al. 1995a). Goedhart et al. (2004) reported that in February 1999, there was an increase in the 6.7-GHz methanol maser emission at a velocity -5.88 km s^{-1} , which peaked in Nov 1999 in the HartRAO’s Hartebeesthoek 26m single dish maser monitoring program. The sensitive spectrum of the 6.7-GHz methanol masers undertaken as part of the methanol multibeam survey in 2006/2007 (Caswell et al. 2010) shows it to be remarkably similar to the 1991 discovery observation of Menten.

The detection in Hartebeesthoek maser monitoring in early 2015 of a significant flare in a variety of maser transitions associated with NGC6334I was the catalyst for the October 2015 LBA observations to enable a comparison with the pre-flare data. A variety of other follow-up observations were also triggered by the maser flare event and Brogan et al. (2016) and Hunter et al. (2017, 2018) detected an outburst

in the 1.3-mm continuum emission. The NGC6334I maser flaring event was most noticeable over the velocity range -9.0 km s^{-1} to -5 km s^{-1} , which started from 1 Jan 2015 and peaked in August 2015 for the 6.7-GHz class II methanol masers (MacLeod et al. 2018). Hunter et al. were able to compare the dust continuum emission at 1.3 mm observed in 2008 with the Submillimeter Array (SMA) with the 6-cm continuum (VLA, 2011) and the 3-mm and 1.3-mm continuum (ALMA, August 2015) (Brogan et al. 2016), which showed that the NGC6334I protocluster region consists of four primary millimetre sources.

Hunter et al. (2017) found that dust luminosities of sources in the MM1 region increased by nearly 70 times between May 2011 and Aug 2015. They reported that the peak of the outburst in the dust continuum was centred on the MM1-B sub-region and is estimated to coincide with the period when MacLeod et al. (2018) reported an increase in the flux densities in methanol maser in the -9.0 km s^{-1} to -5 km s^{-1} velocity range. Subsequent observations had detected mid-infrared continuum emission post-flare from MM1 indicating an increase in luminosity of approximately 16 compared to

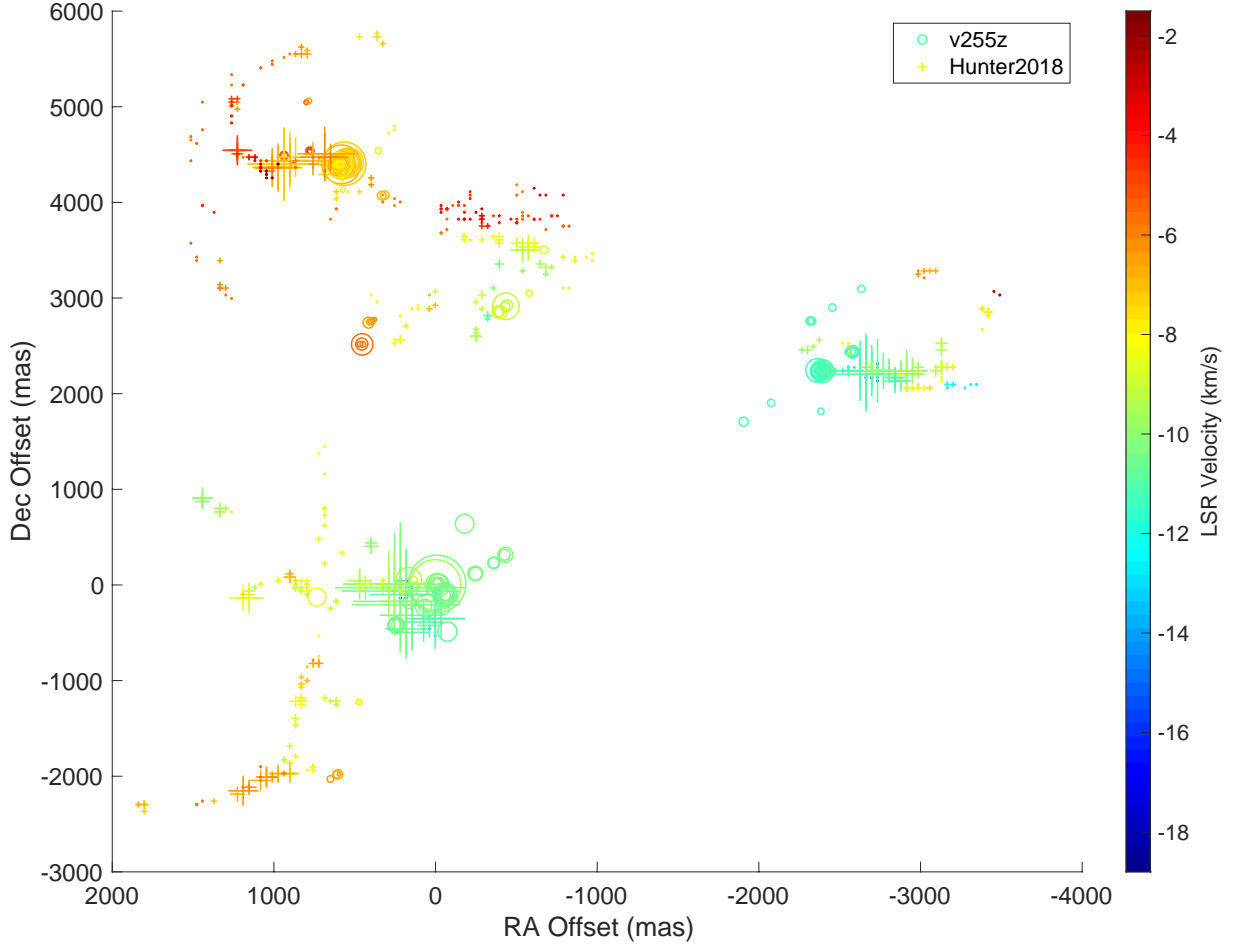


Figure 10. Maser features in the total maser emission in NGC6334I star-forming region for October 2015 and maser features reported by (Hunter et al. 2018) at 6.7 GHz. All maser features are plotted on R. A. and DEC. maps with their velocity information. Maser features from my work are plotted by circles and maser features reported by Hunter 2018 at 6.7 GHz are plotted by "+" sign

pre-flare when MM1 was not detected at $18\mu\text{m}$ wavelength Hunter et al. (2021). At a distance of 1.3 kpc NGC6334I is a relatively nearby cluster/high-mass star formation region, but the complexity and multiplicity of proto-stellar and young-stellar objects of a variety of masses and ages is quite typical. The utility of maser monitoring in detecting and understanding variable accretion rates in high-mass star formation regions requires us to understand in much greater detail how and when the two are linked. The large amount of published multi-wavelength data available for the NGC6334I region makes it an ideal source for such investigations. Hunter et al. (2021), reported the first mid-IR imaging of MM1 post-flare. They found that the outburst in NGC6334I-MM1B exceeded that of other measured mid-IR outbursts, such as that detected towards S255IR-NIRS3 (Caratti o Garatti et al. 2017) by ≥ 3 in both duration and energy. They suggest that it requires a hydrodynamic model which involves heating and expansion of the outer layers of the protostar and could explain the longer decay times seen in NGC6334I-MM1 (Hunter et al. 2021; Larson 1980; Herbig et al. 2003).

MacLeod et al. (2018) observed a 1-2 orders of magnitude in-

crease in the intensity of some class II methanol maser components in NGC6334I on timescales of around 6 months. The presence of interstellar masers implies both suitable physical conditions in the molecular gas (temperature, density, etc), and a sufficient abundance of the relevant molecule with line-of-sight velocity coherence to the observer. Methanol is thought to be produced through grain surface chemistry and released into the gas phase through desorption of ice-grain mantels as they are heated through radiation or shocks (Garrod et al. 2006; Tielens & Whittet 1997; Hudson & Moore 1999; Gibb & Davis 1998). The typical linear scale of class II methanol maser regions in the plane of the sky is around 0.03 pc (Caswell 1997) and as there is little evidence of preferred geometry it is reasonable to assume that most spectral components we see are due to random locations within a volume of molecular gas where there is an unusually high degree of line-of-sight velocity coherence.

The current LBA observations show the emergence of multiple new clusters of 6.7-GHz class II methanol maser emission in the October 2015 epoch. As previously established by Hunter et al. (2017), the new 6.7-GHz class II methanol masers emerged in the molecular

gas surrounding the MM1B millimetre continuum source and [Hunter et al. \(2018\)](#) reported new maser emission from multiple species in the MM1 region. It is interesting to consider what sort of physical conditions may have changed in and around MM1 that made the conditions suitable for the sudden emergence of the 6.7-GHz methanol, other methanol transitions and maser species in the MM1 region. While changes in methanol abundance, gas temperature/density or motions within the molecular gas can produce maser variability they are inconsistent with the timescales and changes in intensity that are observed. It is well-established that the class II methanol masers are radiatively pumped ([Cragg et al. 2005](#); [Sobolev et al. 1997](#)) and the light-travel time for the maser cluster regions are comparable to the observed rise-time for the 2015 NGC6334I maser flare. [Hunter et al. \(2017\)](#) suggested that an unprecedented increase in the temperature of the sub-millimetre dust continuum gave rise to an increase in the radiative pumping in the sub-region MM1, which then resulted in the emergence of new masers. [Hunter et al. \(2018\)](#) suggested that the outburst in the dust continuum heated the dust in the vicinity which then created the ideal conditions for maser emission inversion in already available methanol-rich gas. The reason for the outburst in the millimetre continuum in the MM1B region may be an accretion burst. Other possibilities suggested by [Hunter et al. \(2018\)](#) include a supernova event in MM1 or the merger of two protostars (e.g. [Bally & Zinnecker 2005](#)).

On the basis of our high-resolution imaging data, combined with published methanol monitoring and millimetre continuum data, we suggest that in early 2015 an episodic accretion event in one or more protostellar objects in the MM1 region produced a change in the radiation field in the surrounding molecular gas which "switched-on" class II methanol maser emission in this region. The molecular gas within which MM1 is embedded already had reasonable methanol abundance, as indicated by the 2011 detection of weak thermal emission toward MM1 ([Ellingsen et al. 2018](#)). It has previously been suggested that the luminosity of 6.7-GHz methanol masers and the presence of rarer class II methanol transitions can be used as an indicator of the evolutionary stage of a high-mass star formation region (e.g. [Breen et al. 2010](#); [Ellingsen et al. 2011](#)). In this scenario sources with low-luminosity 6.7-GHz methanol masers are sources at an early evolutionary stage and sources like NGC6334I with high-luminosity and detected emission in a plethora of other class II methanol transitions are the most evolved. The sudden appearance of relatively luminous 6.7-GHz and 12.2-GHz methanol masers along with the relatively rare 23.1-GHz transition in the NGC6334I-MM1 region would appear to be inconsistent with the suggestion of the methanol masers providing a reliable evolutionary timeline, however, there are a number of potential explanations. One is that for cluster star formation there will always be objects spanning a range of ages and that the masers are useful only as an evolutionary clock for the cluster, not individual sources within the cluster. Another is that MM1 in its typical state hosts only relatively low-luminosity 6.7-GHz methanol masers, which were present prior to 2015, but not detectable in either single-dish or interferometric observations due to dynamic range limitations created by the nearby masers in MM3 and MM2 with overlapping velocity ranges. One relatively easy way to test this would be to make sensitive interferometric observations of class II methanol transitions such as the 12.2, 19.9, 23.1, 37.7 and 38.3 GHz and compare the data with the published pre-flare distribution of these transitions. Given the absence of any evidence for class II methanol maser emission associated with MM1 for the nearly 25 years for which we have data prior to the 2015 flare event, their presence 10 years post-flare would indicate either a permanent shift in the radiation field surrounding MM1, or a very long post-flare decline phase for the masers. The

latter has been proposed by [Hunter et al. \(2021\)](#) who compared mid-infrared data with the hydrodynamic model of [Meyer et al. \(2017\)](#) and infer from them a flare duration of 40-130 years. A repeat of the 2016 millimetre continuum emission observations would also be beneficial as it would give a more direct and holistic picture of the changes in the radiation field in NGC6334I. That the class II methanol masers associated with both MM2 and MM3 have changed significantly in the period during and post-flare compared to the approximately 25 years prior to that is suggestive that the 2015 flare has impacted a relatively large volume of the NGC6334I cluster region. The maser emission provides a complementary method of investigating the radiation field. The millimetre continuum observations ([Hunter et al. 2018](#)) have angular resolution several orders of magnitude lower than centimetre wavelength VLBI and their interpretation is complicated by optical depth effects. Maser studies can thus complement millimetre and infrared continuum data by providing information at select locations at much higher resolution, although determining the physical conditions of the masing gas requires observations of multiple transitions and inference in the context of a theoretical model of the masing process.

We have also compared the LBA 6.7 methanol maser distribution for NGC6334I with that observed by [Ellingsen et al. \(2018\)](#) in the 37.7-GHz and 38.3-GHz class II methanol maser transitions (figure 6 in [Ellingsen et al. \(2018\)](#)). The [Ellingsen et al.](#) observations were made with the ATCA on March 24, 2011. Figure 6 in [Ellingsen et al. \(2018\)](#) shows that for both the 37.7-GHz and 38.3-GHz methanol transitions maser emission was detected only towards the MM2 and MM3 regions. The [Ellingsen et al. \(2018\)](#) results show weak thermal emission from both transitions, which peaks at a velocity of around -7 km s^{-1} towards MM1, but no maser emission. Given that the 37.7/38.3 GHz observations were made approximately 4 years prior to the NGC6334I flaring event these data are consistent with the widespread presence of gas-phase methanol in the NGC6334I region, but a lack of widespread inversion of class II methanol transitions near MM1 prior to 2015. Similarly, [Krishnan et al. \(2013\)](#) made interferometric images of the 19.9- and 23.1-GHz methanol maser distribution in NGC6334I utilising ATCA observations from March 27, 2005, with those transitions only being detected close to the strongest 6.7-GHz emission from the MM3 region at that epoch. The [Krishnan et al. 23.1-GHz](#) observations included the velocity range where the strongest class II methanol maser emission was detected during the 2015 flare and the Hartebeesthoek monitoring of [MacLeod et al. \(2018\)](#) shows emission with a peak intensity of around 5 Jy at velocities greater than -10 km s^{-1} . The 2005 ATCA observations of the 23.1-GHz transition had an RMS noise level of 30 mJy, so we can be confident that any emission from this transition at that time was at least an order of magnitude weaker than in 2015. Sensitive Parkes observations of the 23.1-GHz methanol masers from the NGC6334I region made in 2001 also show no sign of emission at velocities greater than -10 km s^{-1} at that epoch ([Cragg et al. 2004](#)).

[Goedhart et al. \(2004\)](#) reported a flaring event in the 6.7-GHz methanol masers in the NGC6334I protocluster. They reported the single dish maser monitoring data from Hartebeesthoek 26m observations between 28 Feb 1999 to 27 March 2003. Their results show flaring in a velocity component at -5.88 km s^{-1} which peaked in Nov 1999. [Hunter et al. \(2018\)](#) and [MacLeod et al. \(2018\)](#) suggested that the 1999 flare and the 2015 flare may originate from the same place in the MM1 region. While we cannot rule out this possibility there are no interferometric observations prior to 2015 which show methanol maser emission from the MM1 region and the velocity range of the 6.7-GHz methanol masers in MM3 extends to -5.9 km s^{-1} . There was also an earlier maser flaring event reported by [Weaver et al.](#)

(1968) which shows variability in ground-state OH masers in 1965. MacLeod et al. (2018) have hypothesised that the flaring events in NGC6334I are periodic and predict the next flaring event may occur in late 2026. However, both interferometric and single dish maser monitoring studies suggest that the earlier maser variability episode reported by Goedhart et al. (2004) and Weaver et al. (1968) were less dramatic than the 2015 flaring event, the impact of which is being observed 5 years later, as shown in the March 2020 observations.

The connection between 6.7-GHz methanol maser flares and episodic accretion events in high-mass star formation regions has been established in three cases S255-IR3, NGC6334I and G358.93-0.03. The first two events provided significant impetus for large-scale monitoring of the 6.7-GHz methanol maser transition. The variability of the class II methanol masers is typically observed to be less dramatic than for the 22-GHz water masers (Caswell et al. 1995a; Ellingsen et al. 2007), although periodic emission is detected in some sources (e.g. Goedhart et al. 2004). The reliable identification of maser flaring events triggered by episodic accretion is still being refined, but the key characteristics seem to be a rapid and dramatic increase in the intensity of the 6.7-GHz transition and the appearance of emission from the rarer class II transitions. These phenomena were observed both in NGC6334I and subsequently in G358.93-0.03 (Breen et al. 2019; Chen et al. 2020; Burns et al. 2020). G358.93-0.03 is a much lower luminosity 6.7-GHz methanol maser source that showed a dramatic increase in its intensity in a short period in early 2019 (Sugiyama et al. 2019). The early detection of this flaring event and follow-up coordinated by the M2O collaboration enabled the detection of a range of rare maser transitions towards G358.93-0.03, many of which were only detectable for a period of weeks (Breen et al. 2019; Chen et al. 2020). Comparison of targeted mid-infrared observations with archival data confirmed an episodic accretion event in G358.93-0.03, but associated with a less massive protostellar object than NGC6334I-MM1 (Stecklum et al. 2021). Developing a more detailed understanding of the link between maser variability and episodic accretion events requires both theoretical studies of the chemistry and masers and observational data to inform, constrain and test the theoretical investigations. This work has commenced (Guadarrama et al. 2024), but is currently in its early stages

5 CONCLUSIONS

The unprecedented outburst and maser flaring event in the NGC6334I protocluster presents an excellent opportunity to study the phenomenon of cluster star formation in the Milky Way. Our data are consistent with the maser flare being produced by a sudden change in the radiation field in a region of molecular gas which already has relatively high methanol abundance. Further high-resolution interferometric observations of methanol and other maser transitions, as well as single dish monitoring observations of the masers and millimetre through mid-infrared continuum observations, will be a key to better understanding the processes which govern variable accretion rates in high-mass star-forming regions.

ACKNOWLEDGEMENTS

This research was supported by the Australian Research Council (ARC) Discovery grants No. DP180101061 and DP230100727. The LBA is part of the Australia Telescope National Facility which is funded by the Australian Government for operation as a National

Facility managed by CSIRO and the University of Tasmania. This research has made use of NASA's Astrophysics Data System Abstract Service.

DATA AVAILABILITY

The correlator FITS files and associated metadata for the Long Baseline Array data underlying this article are available via the Australia Telescope Online Archive under experiment code V255 sessions I, J, Z and AI.

REFERENCES

- Bally J., Zinnecker H., 2005, *AJ*, **129**, 2281
- Batrla W., Matthews H. E., Menten K. M., Walmsley C. M., 1987, *Nature*, **326**, 49
- Beuther H., Walsh A. J., Thorwirth S., Zhang Q., Hunter T. R., Megeath S. T., Menten K. M., 2008, *A&A*, **481**, 169
- Breen S. L., Ellingsen S. P., Caswell J. L., Lewis B. E., 2010, *MNRAS*, **401**, 2219
- Breen S. L., Sobolev A. M., Kaczmarek J. F., Ellingsen S. P., McCarthy T. P., Voronkov M. A., 2019, *ApJ*, **876**, L25
- Brogan C. L., Hunter T. R., Cyganowski C. J., Chandler C. J., Friesen R., Indebetouw R., 2016, *ApJ*, **832**, 187
- Brogan C. L., et al., 2018, *ApJ*, **866**, 87
- Burns R. A., et al., 2020, *Nature Astronomy*, **4**, 506
- Caratti o Garatti A., et al., 2017, *Nature Physics*, **13**, 276
- Caswell J. L., 1997, *MNRAS*, **289**, 203
- Caswell J. L., Vaile R. A., Ellingsen S. P., 1995a, *Publ. Astron. Soc. Australia*, **12**, 37
- Caswell J. L., Vaile R. A., Ellingsen S. P., Whiteoak J. B., Norris R. P., 1995b, *MNRAS*, **272**, 96
- Caswell J. L., et al., 2010, *MNRAS*, **404**, 1029
- Chen X., et al., 2020, *Nature Astronomy*, **4**, 1170
- Chibueze J. O., et al., 2014, *ApJ*, **784**, 114
- Chibueze J. O., MacLeod G. C., Vorster J. M., Hirota T., Brogan C. L., Hunter T. R., van Rooyen R., 2021, *ApJ*, **908**, 175
- Cragg D. M., Sobolev A. M., Ellingsen S. P., Caswell J. L., Godfrey P. D., Sali S. V., Dodson R. G., 2001, *MNRAS*, **323**, 939
- Cragg D. M., Sobolev A. M., Caswell J. L., Ellingsen S. P., Godfrey P. D., 2004, *MNRAS*, **351**, 1327
- Cragg D. M., Sobolev A. M., Godfrey P. D., 2005, *MNRAS*, **360**, 533
- Deller A. T., et al., 2011, *PASP*, **123**, 275
- Ellingsen S. P., 2002, in Migenes V., Reid M. J., eds, *IAU Symposium Vol. 206, Cosmic Masers: From Proto-Stars to Black Holes*. p. 151 ([arXiv:astro-ph/0110127](https://arxiv.org/abs/astro-ph/0110127)), doi:10.48550/arXiv.astro-ph/0110127
- Ellingsen S. P., et al., 1996a, *arXiv e-prints*, pp astro-ph/9604024
- Ellingsen S. P., Norris R. P., McCulloch P. M., 1996b, *MNRAS*, **279**, 101
- Ellingsen S. P., Voronkov M. A., Cragg D. M., Sobolev A. M., Breen S. L., Godfrey P. D., 2007, in Chapman J. M., Baan W. A., eds, *IAU Symposium Vol. 242, Astrophysical Masers and their Environments*. pp 213–217 ([arXiv:0705.2906](https://arxiv.org/abs/0705.2906)), doi:10.1017/S1743921307012999
- Ellingsen S. P., Breen S. L., Sobolev A. M., Voronkov M. A., Caswell J. L., Lo N., 2011, *ApJ*, **742**, 109
- Ellingsen S. P., Voronkov M. A., Breen S. L., Caswell J. L., Sobolev A. M., 2018, *MNRAS*, **480**, 4851
- Evans Neal J. I., et al., 2009, *ApJS*, **181**, 321
- Feigelson E. D., Martin A. L., McNeill C. J., Broos P. S., Garmire G. P., 2009, *AJ*, **138**, 227
- Forster J. R., Caswell J. L., 1989, *A&A*, **213**, 339
- Garrod R., Park I. H., Caselli P., Herbst E., 2006, *Faraday Discussions*, **133**, 51
- Gaume R. A., Mutel R. L., 1987, *ApJS*, **65**, 193
- Gibb A. G., Davis C. J., 1998, *MNRAS*, **298**, 644
- Goedhart S., Gaylard M. J., van der Walt D. J., 2004, *MNRAS*, **355**, 553

- Guadarrama R., Vorobyov E. I., Rab C., Güdel M., Caratti o Garatti A., Sobolev A. M., 2024, *A&A*, 684, A51
- Hartmann L., Kenyon S. J., 1996, *ARA&A*, 34, 207
- Harvey P. M., Gatley I., 1983, *ApJ*, 269, 613
- Haschick A. D., Baan W. A., 1989, *ApJ*, 339, 949
- Haschick A. D., Baan W. A., Menten K. M., 1989, *ApJ*, 346, 330
- Haschick A. D., Menten K. M., Baan W. A., 1990, *ApJ*, 354, 556
- Herbig G. H., Petrov P. P., Duemmler R., 2003, *ApJ*, 595, 384
- Hudson R. L., Moore M. H., 1999, *Icarus*, 140, 451
- Hunter T. R., Brogan C. L., Megeath S. T., Menten K. M., Beuther H., Thorwirth S., 2006, *ApJ*, 649, 888
- Hunter T. R., Brogan C. L., Cyganowski C. J., Young K. H., 2014, *ApJ*, 788, 187
- Hunter T. R., et al., 2017, *ApJ*, 837, L29
- Hunter T. R., et al., 2018, *ApJ*, 854, 170
- Hunter T. R., et al., 2021, *ApJ*, 912, L17
- Kenyon S. J., Hartmann L. W., Strom K. M., Strom S. E., 1990, *AJ*, 99, 869
- Krishnan V., Ellingsen S. P., Voronkov M. A., Breen S. L., 2013, *MNRAS*, 433, 3346
- Krumholz M. R., 2017, *Star Formation*, doi:10.1142/10091.
- Larson R. B., 1980, *MNRAS*, 190, 321
- Leurini S., Schilke P., Parise B., Wyrowski F., Güsten R., Philipp S., 2006, *A&A*, 454, L83
- Mac Low M.-M., Klessen R. S., 2004, *Rev. Mod. Phys.*, 76, 125
- MacLeod G. C., et al., 2018, *MNRAS*, 478, 1077
- Meeks M. L., Carter J. C., Barrett A. H., Schwartz P. R., Waters J. W., Brown W. E. I., 1969, *Science*, 165, 180
- Menten K. M., 1991, *ApJ*, 380, L75
- Menten K. M., Batrla W., 1989, *ApJ*, 341, 839
- Meyer D. M. A., Vorobyov E. I., Kuiper R., Kley W., 2017, *MNRAS*, 464, L90
- Moran J. M., Rodriguez L. F., 1980, *ApJ*, 236, L159
- Moscadelli L., et al., 2017, *A&A*, 600, L8
- Norris R. P., McCutcheon W. H., Caswell J. L., Wellington K. J., Reynolds J. E., Peng R. S., Kesteven M. J., 1988, *Nature*, 335, 149
- Norris R. P., Whiteoak J. B., Caswell J. L., Wieringa M. H., Gough R. G., 1993, *ApJ*, 412, 222
- Persi P., Tapia M., 2008, in Reipurth B., ed., , Vol. 5, *Handbook of Star Forming Regions*, Volume II. p. 456
- Qiu K., Wyrowski F., Menten K. M., Güsten R., Leurini S., Leinz C., 2011, *ApJ*, 743, L25
- Reid M. J., et al., 2014, *ApJ*, 783, 130
- Rodriguez L. F., Canto J., Moran J. M., 1982, *ApJ*, 255, 103
- Sandell G., 2000, *A&A*, 358, 242
- Sobolev A. M., Cragg D. M., Godfrey P. D., 1997, *A&A*, 324, 211
- Stecklum B., et al., 2021, *A&A*, 646, A161
- Sugiyama K., Saito Y., Yonekura Y., Momose M., 2019, *The Astronomer's Telegram*, 12446, 1
- Tielens A. G. G. M., Whittet D. C. B., 1997, *IAU Symposium*, 178, 45
- Walsh A. J., Burton M. G., Hyland A. R., Robinson G., 1998, *MNRAS*, 301, 640
- Weaver H., Dieter N. H., Williams D. R. W., 1968, *ApJS*, 16, 219
- Willis S., Marengo M., Allen L., Fazio G. G., Smith H. A., Carey S., 2013, *ApJ*, 778, 96
- Wu Y. W., et al., 2014, *A&A*, 566, A17

APPENDIX A: DETAILS OF ALL MASER FEATURES FOR NGC6334I EMISSION FOR ALL EPOCHS

Table A1: Table lists the information for all the measure features extracted in the data reduction for the NGC6334I star-forming region for March 2010 epoch. Columns 1-2 list the feature number and its association with a particular sub-region; columns 3-6 list the LSR velocity, R.A., DEC. and integrated flux of the feature

Feature Number	feature Association	Velocity (kms ⁻¹)	R. A. Offset (mas)	DEC. Offset (mas)	Integrated Flux (Jy beam ⁻¹)
1	MM2	-11.499	-2472.826309	2227.456909	5.81
2	MM2	-11.473	-2533.170517	2159.186341	3.35
3	MM2	-11.374	-2364.274578	2155.728989	11.80
4	MM2	-11.364	-2503.921371	1930.274736	9.11
5	MM2	-11.350	-2287.366421	1845.490744	9.23
6	MM2	-11.322	-2373.798878	2156.358592	14.40
7	MM2	-11.319	-2530.383224	2195.336555	22.10
8	MM2	-11.298	-2376.946066	2330.817096	10.20
9	MM2	-11.276	-2360.811191	2250.616462	17.00
10	MM2	-11.227	-2389.125431	2153.083746	25.30
11	MM2	-11.188	-2411.281921	2327.033166	14.20
12	MM2	-11.177	-2367.577711	2246.295686	233.00
13	MM2	-11.172	-2407.694568	2149.681247	16.90
14	MM2	-11.144	-2426.028737	2411.946066	15.30
15	MM2	-11.129	-2405.204795	2238.906219	50.20
16	MM2	-11.123	-2391.684397	2239.600528	20.70
17	MM2	-11.078	-2420.727054	2148.180142	11.40
18	MM2	-11.042	-2421.225025	2231.044569	12.20
19	MM2	-11.034	-2428.747443	2235.703355	16.30
20	MM2	-10.998	-2408.222443	2238.077589	32.40
21	MM2	-10.942	-2400.393321	2242.556118	21.50
22	MM2	-10.915	-2448.615933	2237.112482	13.40
23	MM2	-10.844	-2385.235967	2335.021698	3.74
24	MM3	-10.771	-73.272863	-485.852503	80.20
25	MM3	-10.749	876.527065	478.920398	5.73
26	MM2	-10.744	-2461.727447	2239.474076	17.50
27	MM3	-10.654	-67.876763	-200.658357	12.20
28	MM3	-10.639	-46.726045	-106.601852	113.00
29	MM3	-10.610	-50.873075	-103.580481	12.50
30	MM3	-10.599	-56.146080	-105.408705	145.00
31	MM3	-10.358	-43.949651	-75.895697	35.30
32	MM3	-10.332	-17.438501	8.495997	16.70
33	MM3	-10.288	-45.275446	-81.271289	58.20
34	MM3	-10.266	-56.504285	-66.210008	51.90
35	MM3	-10.244	-36.258666	4.511296	40.50
36	MM3	-10.244	-58.668890	-77.856609	54.60
37	MM3	-10.238	-22.684602	9.593591	59.60
38	MM3	-10.221	-9.581065	16.556627	24.00
39	MM2	-10.200	-2568.260563	2223.409765	17.30
40	MM3	-10.182	-9.973585	10.290471	271.00
41	MM3	-10.135	-8.376544	-245.085114	6.22
42	MM2	-10.127	-2539.426185	2232.296119	9.24
43	MM2	-10.105	-2625.868691	2152.789992	11.50
44	MM3	-10.069	-10.969779	-3.971104	11.10
45	MM2	-10.069	-2564.677266	2223.636945	13.00
46	MM2	-10.031	-2632.512698	2241.019476	5.92
47	MM2	-10.019	-2621.664157	2240.601242	5.66
48	MM2	-10.003	-2584.245726	2315.909172	6.11
49	MM2	-10.003	-2573.242120	2314.089703	8.29
50	MM2	-9.985	-2568.721110	2229.057938	7.47
51	MM2	-9.981	-2547.810544	2318.327670	9.09
52	MM2	-9.959	-2608.242106	2246.833534	3.14
53	MM2	-9.959	-2596.362815	2245.858724	3.57

54	MM2	-9.928	-2549.129189	2229.228784	7.12
55	MM3	-9.824	-23.679794	-88.130932	5.31
56	MM3	-9.805	-12.933492	5.459857	2.82
57	MM3	-9.783	83.555537	-56.283225	48.90
58	MM3	-9.761	0.858188	4.333063	5.04
59	MM3	-9.723	-1.987340	-4.956277	23.70
60	MM3	-9.698	7.104589	-1.918821	9.42
61	MM3	-9.652	-165.251635	-49.995291	10.40
62	MM3	-9.622	-6.394887	1.493434	4.54
63	MM3	-9.612	-0.042783	-0.158599	129.00
64	MM3	-9.542	165.025781	50.332232	48.70
65	MM3	-9.527	172.331635	46.660508	3.69
66	MM2	-9.322	-2764.42734	2535.737168	2.34
67	MM3	-9.235	548.979752	-1824.108722	2.04
68	MM2	-9.037	-2748.26989	2262.438775	6.68
69	MM3	-9.037	721.713729	-54.553189	2.23
70	MM2	-9.008	-2754.76552	2266.170004	2.98
71	MM3	-8.971	481.087170	23.836440	1.28
72	MM3	-8.927	140.087670	45.764818	7.00
73	MM3	-8.884	133.784600	-14.718743	1.06
74	MM3	-8.883	126.392205	-11.667326	11.60
75	MM3	-8.730	708.730350	-96.158946	6.67
76	MM3	-8.708	746.185176	-124.969544	1.07
77	MM3	-8.708	705.839031	-101.074094	7.54
78	MM3	-8.576	737.237897	-120.902634	4.30
79	MM3	-8.510	567.807839	-175.763969	8.35
80	MM3	-8.488	206.012384	862.979472	2.17
81	MM3	-8.488	596.831210	994.523311	2.18
82	MM3	-8.482	733.431070	-125.347563	59.90
83	MM3	-8.313	464.357020	-1220.254117	3.55
84	MM3	-8.292	740.116740	-130.138510	5.20
85	MM3	-8.181	452.853942	61.062749	1.23
86	MM3	-8.005	471.490424	-1223.624929	3.85
87	MM3	-7.930	746.915050	49.153644	0.62
88	MM3	-7.874	750.336577	-125.398610	7.57
89	MM2	-7.742	-2976.02027	2870.709027	7.01
90	MM3	-7.413	509.682589	85.966720	5.02
91	MM3	-7.369	347.900046	-2023.312845	2.10
92	MM3	-7.347	513.082289	-1972.761399	23.10
93	MM3	-7.347	522.160460	-1977.426750	2.16
94	MM3	-7.186	507.840428	94.452633	0.76
95	MM3	-7.184	589.855902	-1969.865030	2.02
96	MM3	-7.106	629.657459	-1987.981231	0.95
97	MM3	-7.047	515.404579	92.411717	2.72
98	MM3	-7.040	520.813745	-1994.356081	1.67
99	MM3	-6.933	615.061189	-1981.326689	10.50
100	MM3	-6.864	659.708125	-2020.389241	1.59
101	MM3	-6.864	684.563182	-1918.393166	0.99
102	MM3	-6.842	648.407595	-2020.035620	2.48
103	MM3	-6.820	668.716100	-2029.311729	1.02
104	MM3	-6.738	610.923767	-1979.441727	10.10
105	MM3	-6.381	650.804887	-2026.798346	2.60
106	MM3	-6.337	686.136828	-2028.616618	0.94

Table A2: Table lists the information for all the measure features extracted in the data reduction for the NGC6334I star-forming region for the July 2010 epoch. Columns 1-2 list the feature number and its association with a particular sub-region; columns 3-6 list the LSR velocity, R.A., DEC. and integrated flux of the feature

Feature Number	feature Association	Velocity (kms ⁻¹)	R. A. Offset (mas)	DEC. Offset (mas)	Integrated Flux (Jy beam ⁻¹)
1	MM2	-11.612	-2483.033952	2229.044364	0.66
2	MM2	-11.524	-2304.709525	2286.687010	3.65
3	MM2	-11.524	-2293.835419	2279.895517	2.73
4	MM2	-11.502	-2589.443810	2078.522427	3.09
5	MM2	-11.502	-2417.019690	2172.457858	9.49
6	MM2	-11.491	-2350.971415	2242.419784	4.24
7	MM2	-11.460	-2372.650449	2215.655173	34.80
8	MM2	-11.458	-2507.389293	2022.525579	7.73
9	MM2	-11.436	-2314.547410	2294.818996	7.11
10	MM2	-11.421	-2388.987039	2162.437143	7.39
11	MM2	-11.414	-2350.048286	2475.445241	4.98
12	MM2	-11.392	-2326.460368	2476.380583	5.92
13	MM2	-11.392	-2332.373136	2475.943942	6.47
14	MM2	-11.387	-2552.168048	2165.329807	18.00
15	MM2	-11.378	-2324.984445	2298.986899	41.40
16	MM2	-11.370	-2211.950192	2195.727232	10.70
17	MM2	-11.370	-2310.846831	2288.095944	12.50
18	MM2	-11.370	-1589.251998	2273.446868	4.82
19	MM2	-11.370	-2179.394642	2306.951804	5.79
20	MM2	-11.370	-2295.238075	2560.587488	7.68
21	MM2	-11.355	-2403.610088	2165.393324	9.34
22	MM2	-11.348	-2535.359631	1934.436931	13.10
23	MM2	-11.348	-2093.715254	2214.490470	8.51
24	MM2	-11.346	-2373.293011	2249.887982	10.60
25	MM2	-11.343	-2162.359171	2284.364899	7.31
26	MM2	-11.334	-2385.821610	2223.406356	16.40
27	MM2	-11.326	-2196.117554	2315.070879	9.76
28	MM2	-11.326	-1885.950114	2145.142762	10.10
29	MM2	-11.282	-2221.354185	2196.895026	12.80
30	MM2	-11.282	-2503.037343	2247.887426	18.90
31	MM2	-11.282	-2320.323477	2794.691690	7.61
32	MM2	-11.260	-2358.285710	2244.301185	64.40
33	MM2	-11.254	-2380.833024	2215.925348	22.00
34	MM2	-11.249	-2496.202084	2010.281671	15.30
35	MM2	-11.238	-2346.778931	2300.698851	7.10
36	MM2	-11.222	-2565.134820	2165.614281	21.20
37	MM2	-11.216	-2172.016118	2290.199758	8.72
38	MM2	-11.216	-2305.073250	2281.189126	14.60
39	MM2	-11.198	-2366.696082	2245.056881	99.00
40	MM2	-11.194	-2333.929085	2297.565978	35.10
41	MM2	-11.129	-2527.086871	1928.917246	11.30
42	MM2	-11.128	-2409.194839	2240.078148	29.80
43	MM2	-11.107	-2554.381823	1935.026914	8.09
44	MM2	-11.092	-2312.155623	2282.436497	9.26
45	MM2	-11.078	-2394.510470	2157.296494	23.50
46	MM2	-10.975	-2551.672637	1842.825516	5.07
47	MM2	-10.953	-2405.354618	2236.828774	8.95
48	MM2	-10.909	-2386.977848	2153.452795	3.37
49	MM2	-10.821	-2454.093669	2238.702658	10.20
50	MM3	-10.821	-527.155939	-54.799659	3.48
51	MM3	-10.799	-74.087087	-486.639876	43.20
52	MM3	-10.799	-82.727990	-515.962755	3.91
53	MM3	-10.799	-126.551213	-558.892448	4.94
54	MM3	-10.777	-93.283631	-510.250198	14.00
55	MM3	-10.777	-271.860900	-566.205078	5.53
56	MM3	-10.755	-66.691984	-485.575282	30.00
57	MM3	-10.755	-39.656279	-111.133878	10.40
58	MM3	-10.746	-265.399954	-562.751030	5.94
59	MM2	-10.744	-2462.871419	2238.691785	6.78

60	MM3	-10.740	-13.271724	-452.378233	4.43
61	MM3	-10.733	121.278523	-442.505140	7.31
62	MM3	-10.720	-273.895050	-559.159996	6.45
63	MM3	-10.711	28.291529	-93.133494	7.04
64	MM3	-10.668	-94.950541	-187.475923	15.50
65	MM3	-10.646	-3.555337	-62.288217	7.99
66	MM3	-10.624	-106.942931	-182.333889	16.40
67	MM3	-10.624	-13.226343	-54.373577	18.10
68	MM3	-10.623	-49.501876	-105.312568	179.00
69	MM3	-10.580	-57.846049	-104.174851	24.80
70	MM3	-10.404	-54.201476	-96.159683	32.90
71	MM3	-10.404	-220.641138	-62.880000	20.90
72	MM3	-10.404	25.218156	471.370576	12.40
73	MM3	-10.382	30.030153	-24.130805	20.10
74	MM3	-10.382	-151.123363	13.762132	26.20
75	MM3	-10.360	-210.211309	-69.222024	30.40
76	MM3	-10.360	29.725550	64.855667	16.70
77	MM3	-10.360	-72.113315	-66.067523	22.50
78	MM3	-10.347	-17.865022	7.102746	30.90
79	MM3	-10.316	37.186464	-29.420676	16.60
80	MM3	-10.279	-56.734751	-72.788025	43.40
81	MM3	-10.272	-64.071186	-70.685385	74.80
82	MM3	-10.258	-34.647636	3.075285	13.20
83	MM3	-10.251	-29.172863	-4.113186	20.10
84	MM3	-10.250	-52.133307	-76.583405	64.10
85	MM3	-10.218	-15.117442	-11.368792	11.00
86	MM3	-10.214	-147.516291	13.122030	8.98
87	MM2	-10.185	-2577.534705	2228.728886	14.60
88	MM3	-10.167	-19.462593	14.976442	25.60
89	MM3	-10.163	-215.106417	-63.034566	10.70
90	MM3	-10.162	-11.763260	10.053026	196.00
91	MM3	-10.145	-7.731780	16.544718	13.70
92	MM3	-10.141	36.519321	-164.373164	9.14
93	MM2	-10.116	-2635.195778	2241.549053	14.50
94	MM3	-10.075	-11.298711	-3.958598	14.60
95	MM2	-10.075	-2574.187357	2228.874939	10.30
96	MM3	-10.024	-6.103345	7.467235	96.40
97	MM2	-10.009	-2583.532765	2234.325490	9.01
98	MM2	-9.993	-2639.296301	2245.427040	12.00
99	MM2	-9.987	-2570.870992	2229.753619	6.03
100	MM2	-9.943	-2548.925370	2228.882136	6.62
101	MM2	-9.899	-2567.459209	2231.090648	3.23
102	MM3	-9.789	83.524744	-56.317152	52.40
103	MM3	-9.775	115.587159	30.851602	5.97
104	MM3	-9.724	550.991271	-763.218564	4.08
105	MM3	-9.713	6.566309	-3.655984	25.00
106	MM3	-9.702	659.902378	1478.524757	3.96
107	MM3	-9.658	-165.568669	-50.029814	8.20
108	MM3	-9.635	0.002872	-0.163574	129.00
109	MM3	-9.526	165.225416	50.395464	50.30
110	MM3	-9.526	322.401783	88.415297	3.26
111	MM3	-9.515	171.785270	46.208896	3.60
112	MM3	-9.504	-11.827648	6.406095	2.21
113	MM2	-9.087	-2781.559902	2210.767050	1.62
114	MM2	-9.065	-2747.454743	2262.187052	7.73
115	MM3	-8.955	140.409942	45.950221	5.65
116	MM3	-8.911	119.175705	-8.995158	1.35
117	MM3	-8.889	126.802972	-11.318594	10.30
118	MM3	-8.771	706.314227	-101.087203	5.62
119	MM3	-8.747	709.583427	-95.880562	4.55
120	MM3	-8.736	700.806806	-94.959031	1.37
121	MM3	-8.648	738.578276	-122.292699	2.75

122	MM3	-8.648	942.685336	-48.934151	2.59
123	MM3	-8.582	517.530259	-265.205518	2.97
124	MM3	-8.560	564.125615	-182.492675	3.45
125	MM3	-8.545	482.162631	-121.036036	2.05
126	MM3	-8.538	733.955872	-125.197335	45.90
127	MM3	-8.538	555.314279	-177.018593	4.25
128	MM3	-8.538	865.346574	-112.273848	3.78
129	MM3	-8.538	891.861371	-87.127884	3.43
130	MM3	-8.538	839.481426	849.494745	2.53
131	MM3	-8.516	890.679514	-145.606272	2.39
132	MM3	-8.516	562.741578	-406.988787	2.17
133	MM3	-8.516	462.665914	-92.019734	2.34
134	MM3	-8.501	683.692235	854.129509	2.61
135	MM3	-8.501	-821.750748	837.544836	2.03
136	MM3	-8.494	756.212526	-98.650940	2.44
137	MM3	-8.494	833.326799	536.102096	2.03
138	MM3	-8.485	753.335339	-96.307967	5.24
139	MM3	-8.450	687.510603	-169.158724	3.13
140	MM3	-8.428	725.150963	-125.322917	3.56
141	MM3	-8.428	888.647933	519.780833	1.91
142	MM3	-8.406	698.032856	-174.688411	5.07
143	MM3	-8.406	702.392245	-179.587059	4.53
144	MM3	-8.377	708.205966	-178.992771	6.14
145	MM3	-8.350	761.657125	-104.024110	4.12
146	MM3	-8.341	458.691044	-1216.745571	1.14
147	MM3	-8.340	741.771176	-130.175365	5.41
148	MM3	-8.209	735.926740	-131.509045	2.09
149	MM3	-8.129	713.948799	-184.913504	1.72
150	MM3	-8.121	469.746326	-1222.001580	2.41
151	MM3	-8.008	491.107007	-1193.994289	0.71
152	MM3	-7.960	768.211697	-98.673710	1.18
153	MM3	-7.887	771.743448	-98.836552	1.17
154	MM3	-7.858	721.106981	-179.410039	1.60
155	MM3	-7.858	752.133261	-124.558153	3.35
156	MM2	-7.836	-3155.626300	2816.832892	0.68
157	MM2	-7.792	-3164.651577	2819.426178	0.65
158	MM2	-7.792	-2975.745471	2870.974300	2.84
159	MM2	-7.792	-3006.119053	2815.767734	2.09
160	MM2	-7.770	-2956.270236	2897.990823	2.58
161	MM3	-7.399	530.910836	111.718758	1.65
162	MM3	-7.397	481.118890	-2023.966651	6.97
163	MM3	-7.384	505.100051	-1972.919409	1.83
164	MM3	-7.375	324.547669	-2023.828674	1.32
165	MM3	-7.375	514.267599	-1972.584620	5.12
166	MM3	-7.375	532.311896	-1945.534796	10.00
167	MM3	-7.375	314.094530	-2018.139586	1.41
168	MM3	-7.366	584.392979	-1991.586836	1.03
169	MM3	-7.353	394.083089	-1946.882691	1.49
170	MM3	-7.353	646.788365	-1959.669825	2.22
171	MM3	-7.353	1024.234070	661.432908	0.86
172	MM3	-7.309	473.362576	-2026.819456	2.89
173	MM3	-7.257	464.117126	-2022.744195	1.19
174	MM3	-7.140	548.530438	-1969.070340	1.04
175	MM3	-7.089	661.015359	-1982.576674	1.09
176	MM3	-7.008	626.031876	-1951.703369	3.69
177	MM3	-7.002	641.033944	-1961.103343	1.36
178	MM3	-6.936	588.100184	-2034.767013	2.00
179	MM3	-6.924	561.406759	-2023.097483	1.85
180	MM3	-6.914	500.024923	-1955.963253	1.42
181	MM3	-6.914	575.591475	-2033.511273	4.70
182	MM3	-6.913	630.946158	-1954.829820	10.20
183	MM3	-6.892	619.028071	-1980.921207	1.25

184	MM3	-6.892	613.488595	-1950.106461	1.79
185	MM3	-6.881	580.590519	-1893.288293	1.31
186	MM3	-6.870	623.980450	-1984.212004	1.24
187	MM3	-6.848	755.617164	-1821.997770	1.02
188	MM3	-6.584	773.473629	-1946.977285	3.52

Table A3: Table lists the information for all the measure features extracted in the data reduction for the NGC6334I star-forming region for the October 2015 epoch. Columns 1-2 list the feature number and its association with a particular sub-region; columns 3-6 list the LSR velocity, R.A., DEC. and integrated flux of the feature

Feature Number	feature Association	Velocity (kms ⁻¹)	R. A. Offset (mas)	DEC. Offset (mas)	Integrated Flux (Jy beam ⁻¹)
1	MM2	-11.426	-2354.789205	2243.027213	14.70
2	MM2	-11.426	-2363.506992	2236.303520	4.17
3	MM2	-11.404	-2550.967305	2435.696650	3.58
4	MM2	-11.294	-2363.248084	2244.380175	60.00
5	MM2	-11.292	-2370.528519	2238.521218	28.00
6	MM2	-11.287	-2383.166049	1815.333063	4.57
7	MM2	-11.273	-2374.940006	2244.950437	4.21
8	MM2	-11.229	-2075.626232	1904.068771	5.77
9	MM2	-11.229	-2382.101537	2249.409273	12.50
10	MM2	-11.229	-2315.520641	2759.465565	7.09
11	MM2	-11.229	-2567.145947	2438.779714	9.49
12	MM2	-11.204	-2387.640499	2235.926727	35.80
13	MM2	-11.189	-2380.618290	2238.634886	40.40
14	MM2	-11.163	-2322.387245	2759.817382	5.10
15	MM2	-11.163	-2403.871889	2232.345646	8.72
16	MM2	-11.155	-2386.556361	2232.271430	11.10
17	MM2	-11.152	-2577.066001	2433.860311	11.70
18	MM2	-11.119	-2388.116168	2244.830371	8.60
19	MM2	-11.097	-2421.032075	2229.890191	6.09
20	MM2	-11.097	-2327.781240	2760.588344	6.85
21	MM2	-11.097	-2395.108719	2241.598269	5.66
22	MM2	-11.082	-2634.310317	3095.808715	5.43
23	MM2	-11.078	-2400.485899	2234.624721	22.60
24	MM2	-11.075	-2394.089011	2236.093760	57.10
25	MM2	-11.053	-2581.870985	2438.181149	17.40
26	MM2	-11.053	-1905.723238	1706.482899	9.03
27	MM2	-11.009	-2413.954388	2231.341742	11.90
28	MM2	-11.002	-2402.058894	2246.599284	20.80
29	MM2	-10.979	-2454.345289	2900.405852	5.88
30	MM2	-10.979	-2590.686392	2436.132650	7.21
31	MM2	-10.932	-2406.995636	2236.318242	31.60
32	MM2	-10.760	-2462.030327	2237.478457	3.84
33	MM3	-10.746	-73.237319	-487.331052	40.30
34	MM3	-10.658	-48.426139	-109.103272	21.00
35	MM3	-10.636	-56.551175	-108.153715	40.50
36	MM3	-10.614	-358.652776	227.517865	13.80
37	MM3	-10.599	-63.295085	-99.783595	36.70
38	MM3	-10.584	-359.891624	233.431802	13.80
39	MM3	-10.570	-56.765285	-101.980354	63.70
40	MM3	-10.438	243.621710	-424.067579	29.40
41	MM3	-10.409	-69.456192	-87.814199	24.60
42	MM3	-10.372	-3.051211	9.231549	20.20
43	MM3	-10.372	237.458150	-414.362559	13.60
44	MM3	-10.307	253.197824	-414.353247	15.00
45	MM3	-10.307	244.653559	-412.587697	25.20
46	MM3	-10.306	55.317855	-217.090100	55.10

47	MM3	-10.306	-247.745468	117.621139	18.30
48	MM3	-10.277	165.942555	-183.131101	16.00
49	MM3	-10.263	-246.090564	120.439282	23.70
50	MM3	-10.263	-431.615810	314.814635	25.40
51	MM3	-10.262	-180.054785	639.767918	38.00
52	MM3	-10.248	-51.867850	-249.688295	13.40
53	MM3	-10.241	-13.555459	8.744841	41.60
54	MM3	-10.219	-57.295869	-76.572186	30.00
55	MM3	-10.219	65.078023	-218.548654	19.00
56	MM3	-10.183	-6.388329	-0.434050	16.00
57	MM3	-10.183	-20.114876	18.990356	13.70
58	MM3	-10.169	-9.577592	11.075908	361.0
59	MM3	-10.160	-427.565148	315.094218	12.90
60	MM3	-10.021	-11.080107	-3.499921	62.10
61	MM2	-9.880	-2391.304830	2266.745694	5.30
62	MM3	-9.824	83.397234	-56.046797	15.90
63	MM3	-9.685	-0.042028	-0.138938	280.0
64	MM3	-9.494	164.768884	50.536765	70.60
65	MM1-II	-9.213	-441.178010	2920.425512	14.70
66	MM1-II	-9.187	-435.588160	2914.122588	76.50
67	MM1-II	-9.121	-431.400080	2910.171243	9.14
68	MM1-II	-8.967	-670.744800	3506.137614	6.89
69	MM3	-8.902	139.280103	46.260271	8.34
70	MM3	-8.880	125.988484	-11.458890	7.50
71	MM1-II	-8.660	-390.434484	2860.458238	14.40
72	MM1-II	-8.565	-383.283355	2854.336486	13.40
73	MM3	-8.506	734.114477	-126.733203	35.40
74	MM1-II	-8.419	-578.443550	3050.824329	4.41
75	MM1-II	-8.309	-402.934994	2851.412458	17.90
76	MM3	-8.111	469.124457	-1224.190938	2.42
77	MM3	-7.958	473.724871	-1225.854198	3.62
78	MM1-I	-7.936	593.883682	4401.716307	4.78
79	MM1-I	-7.914	609.700485	4395.580990	4.40
80	MM1-I	-7.892	573.031772	4132.954490	2.82
81	MM1-I	-7.892	355.203687	4541.005836	4.15
82	MM1-I	-7.862	588.939024	4393.666472	5.26
83	MM1-I	-7.847	597.584326	4389.842073	71.10
84	MM1-I	-7.694	580.934095	4397.245515	5.53
85	MM1-I	-7.474	560.840875	4415.239451	32.70
86	MM1-I	-7.436	550.101649	4410.280746	93.60
87	MM1-I	-7.343	534.182616	4416.507901	89.80
88	MM1-I	-7.343	545.309438	4421.374681	70.60
89	MM1-I	-7.340	564.765915	4403.569852	205.0
90	MM1-I	-7.321	531.210578	4427.860991	34.20
91	MM1-I	-7.296	551.174664	4420.600415	17.10
92	MM1-I	-7.277	564.736622	4412.451602	13.10
93	MM1-I	-7.205	554.632264	4407.612750	72.20
94	MM1-I	-7.189	536.294687	4424.718332	19.00
95	MM1-I	-7.145	555.577140	4416.282628	38.00
96	MM1-I	-7.079	563.982297	4407.374115	22.20
97	MM1-I	-7.057	314.574288	4075.703702	8.15
98	MM1-I	-7.043	574.231580	4409.231480	13.60
99	MM1-I	-6.969	579.531699	4390.192927	84.30
100	MM1-I	-6.928	573.567926	4398.639083	62.60
101	MM1-I	-6.878	590.635481	4387.847827	9.41
102	MM1-I	-6.842	596.594661	4383.680216	46.90
103	MM1-I	-6.838	582.891094	4397.082399	164.0
104	MM1-I	-6.838	701.563481	4427.330963	7.13
105	MM1-I	-6.829	332.840664	4070.864115	8.23
106	MM1-I	-6.805	589.678816	4395.311511	20.70
107	MM3	-6.772	603.937757	-1980.915149	9.55
108	MM1-I	-6.762	596.730596	4393.775755	9.48

109	MM3	-6.676	612.129507	-1980.942029	5.25
110	MM3	-6.619	596.020133	-1975.030000	1.51
111	MM3	-6.487	650.772116	-2028.827407	4.83
112	MM1-III	-6.465	414.746626	2742.622212	13.00
113	MM1-I	-6.448	783.752230	5060.169098	3.51
114	MM1-III	-6.443	406.636741	2750.507748	4.19
115	MM1-III	-6.281	388.405027	2764.102522	2.12
116	MM1-III	-6.279	397.097589	2758.756657	4.26
117	MM1-III	-6.201	377.350900	2774.629226	1.88
118	MM1-III	-5.828	449.170000	2515.400000	3.68
119	MM1-III	-5.762	466.783705	2518.655475	3.27
120	MM1-III	-5.724	453.766156	2515.285765	49.90
121	MM1-III	-5.699	456.314483	2519.131422	16.10
122	MM1-I	-5.499	799.456950	5047.388432	2.47
123	MM1-I	-5.323	937.690131	4492.288806	7.31
124	MM1-I	-5.301	936.302457	4485.963852	5.04
125	MM1-I	-5.096	879.986897	4388.052703	2.87
126	MM1-I	-5.060	779.089002	4540.142328	6.20
127	MM1-I	-4.994	779.440703	4529.658552	2.99
128	MM1-I	-4.906	771.523489	4537.757511	4.60

Table A4: Table lists the information for all the measure features extracted in the data reduction for the NGC6334I star-forming region for the March 2020 epoch. Columns 1-2 list the feature number and its association with a particular sub-region; columns 3-6 list the LSR velocity, R.A., DEC. and integrated flux of the feature

Feature Number	feature Association	Velocity (kms ⁻¹)	R. A. Offset (mas)	DEC. Offset (mas)	Integrated Flux (Jy beam ⁻¹)
1	MM2	-11.447	-2344.689267	2238.353733	2.62
2	MM2	-11.425	-2352.708713	2241.711972	15.70
3	MM2	-11.398	-2369.039496	2247.275881	3.01
4	MM2	-11.381	-2361.090558	2244.261977	14.00
5	MM2	-11.373	-2217.252140	2529.221178	3.34
6	MM2	-11.315	-2221.417224	2531.696858	5.51
7	MM2	-11.271	-2387.757507	2236.995003	4.49
8	MM2	-11.271	-2373.987947	2229.949344	3.33
9	MM2	-11.249	-2359.823592	2232.146824	3.65
10	MM2	-11.161	-2370.536377	2235.519541	8.07
11	MM2	-11.161	-2119.187333	2569.843333	4.00
12	MM2	-11.158	-2401.509012	2237.835617	27.00
13	MM2	-11.141	-2378.819771	2229.481750	13.30
14	MM2	-11.140	-2385.130000	2247.859980	4.96
15	MM2	-11.139	-2158.504016	2759.780531	8.03
16	MM2	-11.139	-2308.187754	2292.005070	9.85
17	MM2	-11.124	-2366.418995	2226.650808	9.23
18	MM2	-11.117	-2388.095708	2232.843888	6.12
19	MM2	-11.091	-2370.622685	2223.972061	11.50
20	MM2	-11.090	-2393.910549	2232.045766	54.60
21	MM2	-11.089	-2383.985184	2236.916122	3.92
22	MM2	-11.089	-2396.939564	2240.177620	6.64
23	MM2	-11.074	-2539.549548	1947.288023	13.90
24	MM2	-11.069	-2313.674443	2293.120785	11.90
25	MM2	-11.066	-2150.387905	2753.719996	5.27
26	MM2	-11.064	-2170.200658	2763.201523	8.58
27	MM2	-11.051	-2304.601394	2287.886751	14.70
28	MM2	-11.046	-2413.897985	2242.075450	15.00
29	MM2	-10.986	-2406.028484	2235.801826	75.40
30	MM2	-10.934	-2425.005834	2246.428081	3.63
31	MM2	-10.788	-2371.960000	2246.932398	1.99

32	MM2	-10.766	-2453.141479	2231.668923	3.47
33	MM3	-10.744	110.646901	-123.625484	11.40
34	MM3	-10.744	-73.237333	-487.654583	49.30
35	MM3	-10.722	-80.250669	-482.646746	6.60
36	MM3	-10.711	-46.984747	-109.533822	9.72
37	MM2	-10.701	-2461.394810	2236.770722	4.31
38	MM3	-10.679	-10.825967	-320.187304	10.60
39	MM3	-10.671	-51.072116	-106.898460	71.30
40	MM3	-10.657	106.576859	-120.877568	6.55
41	MM3	-10.642	326.380029	708.252520	18.40
42	MM3	-10.635	-55.485681	-103.613773	153.00
43	MM3	-10.621	322.549561	710.889896	24.80
44	MM3	-10.569	-484.716166	213.634836	14.50
45	MM3	-10.569	-64.828634	-93.188606	13.50
46	MM3	-10.547	-488.129923	218.397616	26.90
47	MM3	-10.539	-306.938916	14.627768	6.12
48	MM3	-10.481	-717.564446	472.148004	17.20
49	MM3	-10.481	37.423024	-43.655608	37.00
50	MM3	-10.459	-71.011429	-247.669874	29.60
51	MM3	-10.459	254.890970	493.152166	21.30
52	MM3	-10.459	234.850554	502.496176	18.70
53	MM3	-10.437	-521.460000	257.597518	10.60
54	MM3	-10.415	-2.067840	165.218698	13.30
55	MM3	-10.393	-521.060000	262.930000	10.60
56	MM3	-10.393	-1420.063311	778.740000	10.10
57	MM3	-10.371	239.299521	501.963770	15.80
58	MM3	-10.349	-104.376871	-45.433676	54.60
59	MM3	-10.349	-95.973421	-50.814004	59.00
60	MM3	-10.334	55.043629	-215.503807	15.50
61	MM3	-10.331	233.880324	510.149704	16.30
62	MM3	-10.326	-16.669776	18.469550	17.40
63	MM3	-10.324	-30.046373	19.373219	17.00
64	MM3	-10.291	-294.643024	-589.471017	16.00
65	MM3	-10.284	-52.178677	-253.794828	20.90
66	MM3	-10.271	-57.977735	-248.493540	20.50
67	MM3	-10.262	-196.407817	-89.533820	30.10
68	MM3	-10.262	-153.152962	-294.860679	13.10
69	MM3	-10.261	-215.408976	-531.070638	18.60
70	MM3	-10.261	-22.674734	13.129618	22.70
71	MM3	-10.261	2.341470	-1.879515	73.40
72	MM3	-10.239	7.672253	-9.810822	21.70
73	MM3	-10.218	-76.779314	-57.655723	69.80
74	MM3	-10.204	-2.672749	6.019795	186.00
75	MM3	-10.203	-6.501596	2.660371	34.90
76	MM3	-10.196	219.782779	522.846243	7.94
77	MM3	-10.174	-1281.093273	637.403296	5.92
78	MM3	-10.174	-511.780178	262.835089	6.01
79	MM3	-10.136	-13.871874	8.445068	16.90
80	MM3	-10.108	-4.448205	-7.439274	7.42
81	MM2	-10.077	-2888.462942	1479.054526	5.09
82	MM2	-10.077	-2884.855128	1475.757054	5.72
83	MM3	-10.074	-114.330620	-36.282512	17.00
84	MM3	-10.064	-17.823322	15.714013	21.00
85	MM3	-10.006	-9.113037	10.830142	277.00
86	MM2	-9.910	-2786.294508	1364.479282	2.45
87	MM2	-9.888	-2391.033993	2265.185509	4.51
88	MM3	-9.856	-12.187481	13.145932	9.45
89	MM3	-9.808	83.000433	-56.537820	38.40
90	MM3	-9.757	-108.768476	-45.841420	15.90
91	MM3	-9.735	343.217329	734.869052	16.80
92	MM3	-9.712	6.085113	-6.344917	46.50
93	MM3	-9.703	224.932508	533.310509	22.80

94	MM3	-9.655	244.131104	524.915222	10.20
95	MM3	-9.652	-0.023866	-0.207896	445.00
96	MM3	-9.625	108.756306	45.618579	13.10
97	MM3	-9.515	164.498656	50.499593	74.20
98	MM3	-9.515	171.570305	45.505235	10.20
99	MM3	-9.493	157.410544	57.318543	8.45
100	MM1-II	-9.449	-421.466839	2583.902260	4.34
101	MM1-II	-9.383	-668.403143	3514.066426	23.80
102	MM1-II	-9.375	-568.663343	3566.226497	4.19
103	MM1-II	-9.340	-679.114588	3520.492424	4.28
104	MM1-II	-9.010	-675.652840	3506.023519	15.20
105	MM1-II	-8.966	-682.774106	3509.845651	8.28
106	MM1-II	-8.923	-569.260610	3650.489182	1.98
107	MM3	-8.901	138.826247	46.282541	6.41
108	MM1-II	-8.873	-785.130733	3300.372853	4.72
109	MM3	-8.857	125.472478	-11.907749	8.33
110	MM1-II	-8.747	-655.326104	3590.972104	6.01
111	MM1-II	-8.747	-646.604031	3585.389060	6.77
112	MM3	-8.747	715.927982	-106.807665	5.00
113	MM3	-8.725	710.330425	-99.587137	2.60
114	MM1-II	-8.681	-639.071344	3579.751174	2.44
115	MM3	-8.681	721.720615	-115.081559	3.53
116	MM3	-8.593	728.121830	-121.051244	10.40
117	MM3	-8.506	1085.203032	604.111475	5.51
118	MM1-II	-8.506	-719.374150	3546.517350	3.56
119	MM1-II	-8.471	-711.768526	3540.953873	6.35
120	MM3	-8.471	734.848694	-127.870501	75.60
121	MM3	-8.286	743.706943	-131.573682	7.24
122	MM3	-8.176	468.360376	-1224.892274	4.96
123	MM1-II	-8.176	-345.217625	3672.169272	1.33
124	MM3	-7.957	757.299063	-134.716684	2.08
125	MM3	-7.957	474.168511	-1227.099459	4.07
126	MM3	-7.949	748.355640	-130.218943	3.13
127	MM3	-7.858	752.229230	-127.460656	6.43
128	MM1-I	-7.815	598.788255	4389.730913	19.30
129	MM1-I	-7.815	605.960254	4386.205714	12.20
130	MM1-I	-7.742	590.703536	4394.947211	7.47
131	MM1-I	-7.737	589.740019	4392.567802	3.05
132	MM1-I	-7.650	584.069960	4397.790761	3.90
133	MM1-I	-7.532	419.175581	4123.116757	12.00
134	MM1-I	-7.518	651.170337	4463.942653	9.64
135	MM1-I	-7.515	636.686848	4469.861493	12.30
136	MM1-I	-7.474	627.120168	4473.235985	8.91
137	MM1-I	-7.474	508.829912	4431.199551	11.30
138	MM1-I	-7.473	411.546968	4126.178897	16.50
139	MM1-I	-7.452	394.552360	4133.707422	6.34
140	MM1-I	-7.430	526.479176	4422.340174	22.90
141	MM1-I	-7.424	643.462624	4466.661203	13.20
142	MM1-I	-7.414	536.075013	4418.142012	202.00
143	MM1-I	-7.401	546.506727	4413.199336	80.10
144	MM1-I	-7.390	558.620328	4407.557152	32.90
145	MM1-I	-7.364	517.880953	4427.869695	10.10
146	MM3	-7.342	509.592268	84.840028	5.83
147	MM1-I	-7.328	567.580661	4402.631432	28.00
148	MM1-I	-7.320	319.490600	4069.892561	5.86
149	MM3	-7.298	511.155092	-1976.125124	10.30
150	MM1-I	-7.189	430.552353	4114.260716	5.71
151	MM1-I	-7.189	421.557872	4118.245493	10.30
152	MM1-I	-7.152	554.963963	4406.019950	40.20
153	MM1-I	-7.108	313.910450	4240.813597	12.10
154	MM1-I	-7.097	576.812784	4397.547513	3.50
155	MM1-I	-7.079	559.180851	4403.377470	3.52

156	MM1-I	-7.079	426.197552	4539.023461	5.83
157	MM1-I	-7.079	415.666756	4542.187869	7.11
158	MM1-I	-7.057	553.161442	4311.414278	18.50
159	MM1-I	-7.057	542.294518	4317.776480	16.70
160	MM1-I	-7.035	436.614725	4535.426691	6.95
161	MM1-I	-7.013	576.580000	4394.810000	10.00
162	MM1-I	-7.013	572.920000	4397.565016	15.60
163	MM1-I	-7.004	321.332638	4237.441099	7.14
164	MM1-I	-6.976	461.346437	4525.363253	25.80
165	MM1-I	-6.969	433.192530	4441.777416	29.90
166	MM1-I	-6.969	583.600000	4391.375000	9.93
167	MM1-I	-6.947	579.900363	4393.540960	17.50
168	MM1-I	-6.934	332.674258	4232.878551	6.35
169	MM1-I	-6.925	425.251969	4447.496639	17.60
170	MM3	-6.896	604.470907	-1982.235840	7.40
171	MM1-I	-6.881	444.343516	4440.041003	4.13
172	MM1-I	-6.859	608.110732	4379.739970	5.86
173	MM1-I	-6.845	588.394439	4388.932791	34.70
174	MM1-I	-6.838	457.412880	4097.404046	6.31
175	MM1-II	-6.838	-359.031753	2493.480639	3.59
176	MM3	-6.811	613.429757	-1985.703786	15.80
177	MM1-I	-6.801	596.478182	4382.635193	44.30
178	MM1-I	-6.794	466.816560	4523.512921	17.50
179	MM1-II	-6.772	-336.567199	2577.340244	7.45
180	MM3	-6.706	619.730391	-1990.288109	6.14
181	MM1-I	-6.662	613.463847	4371.253406	4.97
182	MM1-I	-6.662	372.442186	4312.386093	5.55
183	MM3	-6.618	650.144506	-2025.959351	9.66
184	MM1-I	-6.618	340.079961	4510.960700	8.48
185	MM1-I	-6.618	332.647074	4515.790093	4.22
186	MM1-I	-6.596	358.252950	4505.727328	7.55
187	MM3	-6.596	871.362181	-1948.936194	7.84
188	MM1-I	-6.552	346.808542	4508.783808	8.55
189	MM3	-6.549	890.405167	-1862.921815	6.90
190	MM1-I	-6.472	333.769417	4502.903290	3.20
191	MM1-I	-6.428	347.083531	4489.780249	3.45
192	MM1-I	-6.399	363.685658	4486.787193	2.80
193	MM1-I	-6.398	328.461564	4497.470434	26.00
194	MM1-I	-6.389	321.010461	4501.525163	7.43
195	MM1-I	-6.369	314.426156	4509.004404	3.24
196	MM1-I	-6.340	313.994740	4493.140734	6.68
197	MM1-I	-6.333	341.575620	4495.285333	8.90
198	MM1-I	-6.333	320.703204	4486.623979	11.50
199	MM1-I	-6.267	176.729318	4199.946932	2.85
200	MM1-I	-6.223	300.967634	4493.294767	14.00
201	MM1-I	-6.223	409.554889	4540.088667	5.31
202	MM1-I	-6.223	186.833483	4193.138904	2.62
203	MM1-I	-6.190	319.809128	4482.615635	4.95
204	MM1-I	-6.168	312.718534	4486.292351	15.70
205	MM1-I	-6.128	307.728887	4488.494645	23.30
206	MM1-I	-5.015	771.441685	4537.619973	11.80

This paper has been typeset from a \TeX/L\AA\TeX file prepared by the author.